

The new GFDL global atmosphere and land model AM2/LM2: Evaluation with prescribed SST simulations

The GFDL Global Atmospheric Model Development Team¹

Revised for the *Journal of Climate*, February 2004

¹The members of the GFDL Global Atmospheric Model Development Team include Jeffrey L. Anderson⁺, V. Balaji^{\$}, Anthony J. Broccoli^{+,^}, William F. Cooke[%], Thomas L. Delworth⁺, Keith W. Dixon⁺, Leo J. Donner⁺, Krista A. Dunne[#], Stuart M. Freidenreich⁺, Stephen T. Garner⁺, Richard G. Gudgel⁺, C. T. Gordon⁺, Isaac M. Held⁺, Richard S. Hemler⁺, Larry W. Horowitz⁺, Stephen A. Klein^{+*f§}, Thomas R. Knutson⁺, Paul J. Kushner^{+*¥}, Amy R. Langenhorst[%], Ngar-Cheung Lau⁺, Zhi Liang[%], Sergey L. Malyshev[@], P. C. D. Milly[#], Mary J. Nath⁺, Jeffrey J. Ploshay⁺, V. Ramaswamy⁺, M. Daniel Schwarzkopf⁺, Elena Shevliakova[@], Joseph J. Sirutis⁺, Brian J. Soden⁺, William F. Stern⁺, Lori A. Thompson[%], R. John Wilson⁺, Andrew T. Wittenberg^{\$}, and Bruce L. Wyman⁺.

⁺Geophysical Fluid Dynamics Laboratory (GFDL), National Oceanic and Atmospheric Administration, Princeton, New Jersey

^{\$}Atmospheric and Oceanic Sciences Program, Princeton University, Princeton, New Jersey

[%]RS Information Systems, McLean, Virginia, presently at GFDL

[#]U. S. Geological Survey, Princeton, New Jersey

[@]Department of Ecology and Evolutionary Biology, Princeton University, Princeton, New Jersey

[^]Now at the Department of Environmental Sciences, Rutgers University, New Brunswick, New Jersey

[§]Now at the Atmospheric Science Division, Lawrence Livermore National Laboratory, Livermore, California

[¥]Now at the Department of Physics, University of Toronto, Toronto, Ontario, Canada

^{*}Global Atmospheric Model Development Team leaders (2001-2003)

^fCorresponding author: Stephen A. Klein, Geophysical Fluid Dynamics Laboratory/NOAA, Princeton University Forrestal Campus/ US Route 1, P.O.Box 308, Princeton, New Jersey 08542, e-mail: Stephen.Klein@noaa.gov

Abstract

The configuration and performance of a new global atmosphere and land model for climate research developed at the Geophysical Fluid Dynamics Laboratory (GFDL) is presented. The atmosphere model, known as AM2, includes a new gridpoint dynamical core, a prognostic cloud scheme, and a multi-species aerosol climatology, and components from previous models used at GFDL. The land model, known as LM2, includes soil sensible and latent heat storage, groundwater storage, and stomatal resistance. The performance of the coupled model AM2/LM2 is evaluated with a series of prescribed sea-surface temperature (SST) simulations. Particular focus is given to the model's climatology and the characteristics of interannual variability related to El Niño/Southern Oscillation (ENSO).

One AM2/LM2 integration was performed according to the prescriptions of the second Atmospheric Model Intercomparison Project (AMIP II) and data were submitted to the Program for Climate Model Diagnosis and Intercomparison (PCMDI). Particular strengths of AM2/LM2, as judged by comparison to other models participating in AMIP II, include its circulation and distributions of precipitation. Prominent problems of AM2/LM2 include a cold bias to surface and tropospheric temperatures, weak tropical cyclone activity, and weak tropical intraseasonal activity associated with the Madden-Julian oscillation.

An ensemble of 10 AM2/LM2 integrations with observed SSTs for the second half of the twentieth century permits a statistically reliable assessment of the model's response to ENSO. In general, AM2/LM2 produces a realistic simulation of the anomalies in tropical precipitation and extratropical circulation that are associated with ENSO.

1. Introduction

In this report, an overview is presented of the new GFDL global atmosphere and land model known as "AM2/LM2". AM2 and LM2 are, respectively, the atmospheric and terrestrial components of the earth-system model that is under development at GFDL for climate research and climate prediction applications. In developing AM2/LM2, the focus has been on consolidating and improving the various versions of such models that have been used in GFDL's past (Hamilton et al. 1995, Stern and Miyakoda 1995, Delworth et al. 2002). The principal aim is to create a model that realistically represents the dynamic, thermodynamic, and radiative characteristics of the climate system and is suitable for coupling to ocean and sea-ice models without flux adjustment. Balanced against this aim is the need to have a model computationally fast enough so that ensemble multi-century integrations may be performed.

Although AM2/LM2 incorporates many components of previous models used within GFDL, it does represent a substantial break from the past. AM2 includes a new gridpoint atmospheric dynamical core, a multi-species three dimensional aerosol climatology, a fully prognostic cloud scheme and a moist turbulence scheme. LM2 incorporates soil sensible and latent heat storage, groundwater storage, stomatal control of transpiration, and soil- and plant- dependent parameters. These new components have required modification and retuning of components that were carried over from previous models. This has led to a model with more capabilities and potential for growth as well as a model with simulation characteristics generally superior to that of the older GFDL models.

Our model development effort is team-based and involves a broad cross section of exper-

GFDL GAMDT

tise from within and outside of GFDL; this has required a challenging degree of coordination. A simultaneous challenge has been GFDL's transition from vector to parallel computing architectures. To address these challenges, an in-house software framework known as the "Flexible Modeling System" (FMS, <http://www.gfdl.noaa.gov/fms>) has been developed. FMS-based codes are modular, use Fortran 90, and are based on standardized interfaces between component models (i.e. land, atmosphere, ocean, sea-ice). The software conservatively exchanges the fluxes of heat, moisture, and momentum between component models which may have different horizontal grids. The FMS code organization isolates those aspects of the code related to parallel computing to a relatively simple message passing interface (<http://www.gfdl.noaa.gov/~vb/mpp.html>). As a result, scientists developing new code for the model need not learn the intricacies of parallel computing. Using the FMS, it has been possible to rapidly test a variety of model configurations and follow parallel development paths for the atmosphere, ocean, land, and sea-ice models. FMS models have been tested simultaneously on vector and parallel platforms. As a consequence, the transition to a new parallel computing environment was made with relative ease.

Section 2 of the report documents the components of AM2/LM2 as well as the boundary conditions for the experiments performed. Section 3 provides a discussion of AM2/LM2's climatological circulation, hydrology and radiation budget, as well as its variability. A brief comparison of the quality of AM2/LM2's climatology to that of other models is given in section 4 and future plans are discussed in section 5.

2. Model components and boundary conditions for model integrations

The components of AM2/LM2 are described in the following three subsections. For ease of reference, a summary of model components is given in Table 1.

a. Grid-point dynamical core

The hydrostatic, finite difference dynamical core has been developed from models described in Mesinger et al. (1988) and Wyman (1996). The AM2 dynamical core uses the same set of prognostic variables as in these references, but has a different horizontal and vertical grid. The latitude-longitude horizontal grid is the staggered Arakawa B-grid (Arakawa and Lamb 1977) with a resolution of 2.5° longitude by 2° latitude. In the vertical, a hybrid coordinate grid is used; sigma surfaces near the ground continuously transform to pressure surfaces above 250 hPa (Table 2). The model has twenty-four vertical levels with the lowest model level about thirty meters above the surface. There are nine full levels in the lowest 1.5 km above the surface; this relatively fine resolution is needed by the boundary layer turbulence scheme. Aloft the resolution is more coarse with approximately two km resolution in the upper troposphere. Five levels are in the stratosphere, with the top level at about 3 hPa. The prognostic variables are the zonal and meridional wind components, surface pressure, temperature, and tracers. The tracers include the specific humidity of water vapor and three prognostic cloud variables (section 2b3).

The model utilizes a two-level time differencing scheme. Gravity waves are integrated using the forward-backward scheme (Mesinger 1977) and a split time differencing scheme is used for longer advective and physics time steps (Gadd 1978). The advective terms are integrated with a modified Euler backward scheme that has less damping than the full backward scheme (Kuri-

hara and Tripoli 1976). The gravity wave, advective and physics time steps are 200, 600, and 1800 seconds, respectively.

The vertical finite difference scheme used is from Simmons and Burridge (1981), except that the pressure gradient formulation is replaced with the finite-volume method from Lin (1997). Improvements to the flow in the vicinity of steep mountains result from its use. Horizontal advection uses centered spatial differencing. Momentum advection is fourth-order; temperature and tracer advection are second-order. The vertical advection of tracers use a finite-volume scheme (Lin et al. 1994) with the piecewise parabolic method of Colella and Woodward (1984). Grid point noise and the $2\Delta x$ computational mode of the B-grid are controlled with linear fourth-order horizontal diffusion. To prevent spurious diffusion along sloping coordinate surfaces, the diffusive fluxes of heat and moisture are adjusted with a linear correction toward pressure surfaces. A second order Shapiro (1970) filter is applied to the departures from the zonal mean of the zonal wind component and to the total meridional wind component at the top model level to reduce the reflection of waves. Fourier filtering is applied poleward of 60° latitude to damp the shortest resolvable waves so that a longer time step can be taken. The filter is applied to the mass divergence, the horizontal omega-alpha term, the horizontal advective tendencies, and the momentum components.

Although the numerical schemes are designed to conserve total energy, some aspects of the dynamical core do not. These include the horizontal diffusion, the Shapiro filter used at the top level, the time differencing, and the pressure gradient part of the energy conversion term. To guarantee energy conservation for long climate runs, a global energy correction is applied to temperature.

One may ask why this B-grid dynamical core was selected when a standard Eulerian spec-

tral dynamical core is also available within FMS. Throughout the development process, integrations have been performed with this spectral core. Most of the biases that are present simulations with the B-grid core are also present in simulations with a T42 spectral core, including an exaggerated double Intertropical Convergence Zone (ITCZ) structure in the Pacific, the equatorward bias in the position of the North Atlantic westerlies, and the positive bias in Arctic sea level pressure. Overall figures of merit of the sort discussed below are somewhat superior in the B-grid model, which partly reflects that the tuning process focused on integrations with the gridpoint model. One noticeable difference is that South American rainfall is superior in the B-grid model, owing to the difficulty in representing the Andes in a spectral model of this resolution. The deficient spectral model solution occurs despite the use of a sophisticated spectral topography smoothing algorithm (Lindberg and Broccoli 1996). Apart from these considerations, differences in computational efficiency when interchanging dynamical cores are modest at this resolution. For these reasons, the B-grid core has been chosen for the default model.

b. Atmospheric physics

1) RADIATION AND PRESCRIBED OZONE AND AEROSOL CLIMATOLOGIES

The shortwave radiation algorithm follows Freidenreich and Ramaswamy (1999; hereinafter FR99). When this radiation code was first employed in AM2, it was deemed necessary to increase its computational efficiency. As a result, the band structure and the number of exponential-sum fit terms within some bands have been altered, resulting in fewer pseudo-monochromatic columnar calculations. Specifically, the band from 0 to 2500 cm⁻¹ now has one instead of six terms, owing to consideration of CO₂ as the only absorber for this interval; there is one band from 2500 to 4200 cm⁻¹ instead of three, and the total number of terms is reduced from twelve to eight;

there is one band from 4200 to 8200 cm⁻¹ instead of four, and the total number of terms is reduced from twenty-four to nine; the number of terms for the 8200 to 11500 cm⁻¹ band is reduced from seven to five while that for the 11500 to 14600 cm⁻¹ band is reduced from eight to two; there are now three bands between 27500 and 34500 cm⁻¹ instead of five, each with one term. Altogether, the number of bands in the solar spectrum is reduced from twenty-five to eighteen, while the total number of pseudo-monochromatic column calculations required per grid-box is reduced from seventy-two to thirty-eight. This new band structure and the revised exponential-sum fits have been developed and tested with benchmark calculations using the HITRAN 2000 line catalogue (Rothman et al. 2003). Despite the reduced band structure, the maximum error in the clear-sky heating rates remains at the less than 10% as was obtained with the seventy-two term fit. The errors in the shortwave overcast sky heating rates for the water cloud model considered (Slingo 1989) are now about 15%, increased from about 10% for the seventy-two term fit; for ice clouds, the errors tend to be larger (FR99) and for the present parameterization could reach 25%.

The interactions considered by this shortwave parameterization include absorption by H₂O, CO₂, O₃, O₂, molecular scattering, and absorption and scattering by aerosols and clouds. For water clouds, the single-scattering properties in the solar spectrum follow Slingo (1989); for ice clouds, the formulation follows Fu and Liou (1993). To account for the radiation bias that results from using horizontally homogeneous clouds (Cahalan et al. 1994), the cloud liquid and ice water contents are multiplied by 0.85 before calculating both short and longwave radiative properties. Three-dimensional, monthly-mean profiles of aerosol mass concentrations and their optical properties follow Haywood et al. (1999) and Haywood (personal communication). The prescription accounts for sea-salt (low windspeed case) and the natural and anthropogenic components of dust, carbonaceous (black and organic carbon), and sulfate aerosols.

GFDL GAMDT

Ozone profiles follow Fortuin and Kelder (1998) and are based on observations from 1989 to 1991. This climatology has been shown to yield results that represent substantial improvements over those obtained with previous older climatologies used in the GFDL global models (Ramaswamy and Schwarzkopf 2002).

The ocean surface is assumed to be Lambertian, with the albedo a function of the solar zenith angle following the formulation of Taylor et al. (1996).

The band-averaging of the single-scattering parameters in the shortwave parameterization is performed using the thick-averaging technique (Edwards and Slingo 1996). The delta-Eddington technique is employed to compute the layer reflection and transmission based on the single-scattering properties of that layer (FR99). The diffuse incident beam is assumed to be isotropic and its reflection and transmission are computed using an effective angle of 53° , in contrast to the 4-point quadrature scheme used in FR99. The net direct and diffuse quantities in each layer are given by the weighted sum of the clear and overcast sky fractions present in that layer. The total shortwave fluxes and heating rates are computed using an adding scheme (Ramaswamy and Bowen 1994).

The longwave radiation code follows the modified form of the Simplified Exchange Approximation and is also developed and tested using benchmark computations (Schwarzkopf and Ramaswamy 1999). It accounts for the absorption and emission by the principal gases in the atmosphere, including H_2O , CO_2 , O_3 , N_2O , CH_4 , and the halocarbons CFC-11, CFC-12, CFC-113 and HCFC-22. Aerosols and clouds are treated as absorbers in the longwave, with non-grey absorption coefficients specified in the eight spectral bands of the transfer scheme, following the methodology adopted in Ramachandran et al. (2000). For water clouds, the absorption coeffi-

clients follow those employed in Held et al. (1993); for ice clouds, the Fu and Liou (1993) prescription is used.

In both the shortwave and longwave parameterizations, the water vapor continuum is parameterized according to the CKD 2.1 formulation of Clough et al. (1992). Additionally, shortwave and longwave band and continuum parameters are derived using the HITRAN 2000 line catalogue (Rothman et al. 2003).

2) CUMULUS PARAMETERIZATION AND CONVECTIVE MOMENTUM TRANSPORT

Moist convection is represented by the Relaxed Arakawa-Schubert (RAS) formulation of Moorthi and Suarez (1992). In this parameterization, convection is represent by a spectrum of entraining plumes which produce precipitation. Closure is determined by relaxing the cloud work function for each cloud in the spectrum back to a critical value over a fixed time scale. A number of local modifications have been made; these are enumerated below.

- (The fraction of water condensed in the cumulus updrafts which becomes precipitation (known as the precipitation efficiency) is specified to be 0.975 for deep convection and 0.5 for shallow convection. Deep convection is defined as updrafts which detrain at pressure levels above 500 hPa whereas shallow convection is defined as updrafts which detrain beneath 800 hPa. For pressures between 500 and 800 hPa, the precipitation efficiency is linearly interpolated in pressure between the values for deep and shallow convection. This version of RAS lacks cumulus updraft microphysics such as that developed by Sud and Walker (1999).

- The non-precipitated fraction of condensed water, 0.025 for deep convection and 0.5 for shallow convection, is a source of condensate for the prognostic cloud scheme.
- Re-evaporation of convective precipitation is allowed to occur. This version of RAS does not include the effects of convective downdrafts developed in a later version (Moorthi and Suarez 1999).
- The time scale over which the cloud work function is relaxed to a cloud type dependent value is modified so that deep updrafts relax over a time scale of about 12 hours but shallow updrafts relax over a time scale of only 2 hours.
- The cloud type dependent cloud work function is taken from Lord and Arakawa (1980) except that it is reduced to zero for shallow updrafts which detrain below 600 hPa. This change was made to reduce undesirable low cloud behavior on ENSO timescales over the Equatorial Pacific Cold Tongue and a related instability which occurred when an earlier version of AM2/LM2 was coupled with a mixed-layer ocean.

In addition to these changes, deep convection is prevented from occurring in updrafts with a lateral entrainment rate lower than a critical value determined by the depth of the sub-cloud layer (Tokioka et al. 1988). This modification results in general improvements to the distribution of tropical precipitation and an increase in tropical eddy and storm activity. A deleterious effect is a cooling of the upper tropical troposphere by 2K. This constraint is applied only to convective updrafts that detrain above 500 hPa. This constraint has not been applied to shallower updrafts because the resulting decrease in the intensity of shallow convection leads to large increases in tropical low cloud cover to the point that adjusting other model components to achieve radiative balance is too difficult. It is surprising how important weakly entraining updrafts in RAS are to

the distribution of low level cloud cover.

The impact of cumulus convection on the horizontal momentum fields has been represented by adding to the vertical diffusion coefficient for momentum a term of the form:

$$K_{cu} = \gamma M_c d / \rho \quad (1)$$

where K_{cu} is the contribution to the momentum diffusion coefficient from cumulus convection, M_c is the total cumulus mass flux predicted by RAS with units $\text{kg m}^{-2} \text{ s}^{-1}$, d is the depth of convection in meters, ρ is the density of air, and γ is a dimensionless constant with value 0.2. The chosen value of γ is roughly consistent with the cloud resolving model results of Mapes and Wu (2001) who estimate that 10 mm of convective precipitation damps out 40-80% of the mean baroclinic kinetic energy. If one assumes that the horizontal flow has the vertical structure of a full sine wave over a depth of 10 km, then this rate of decay corresponds to the choice of γ between 0.1 and 0.2. In AM2/LM2, this convective momentum transport mutates the tendency of AM2/LM2 to produce a double ITCZ in the tropical Pacific and results in a more realistic regression of zonal surface wind stress in the equatorial Pacific on NINO3 SSTs. A deleterious impact is the sharp reduction of tropical transient eddy activity which has in part motivated the inclusion of the Tokioka modification described above. The marked consequences of including this convective momentum transport on the ENSO spectrum from a coupled model using AM2/LM2 will be described elsewhere.

The choice of a down-gradient diffusive formulation of convective momentum transport in place of the more conventional mass-flux formations (e.g. Gregory et al. 1997), was based in part on concerns regarding numerical stability (Kershaw et al. 2000). Given the uncertainties as to how

convective organization modifies vertical momentum transports and the inability of a large-scale model to address the question of convective organization, it was felt that this simpler scheme might be adequate. One can mimic the tendencies produced by the Gregory et al. (1997) scheme with diffusion if the vertical structure to the mean flow is simple enough (linear in pressure, for example). However, the diffusion coefficients from (1) are larger at low levels than those given by an equivalent mass-flux formulation. The larger momentum tendencies at low levels generated by (1) appear to be important to the advantages obtained from this diffusive formulation in a coupled model.

3) CLOUD SCHEME AND RADIATION BALANCE TUNING

Large-scale clouds are parameterized with separate prognostic variables for specific humidity of cloud liquid and ice. Cloud microphysics are parameterized according to Rotstayn (1997) with an updated treatment of mixed phase clouds (Rotstayn et al. 2000). Fluxes of large-scale rain and snow are diagnosed and the amount of precipitation flux inside and outside of clouds is tracked separately (Jakob and Klein 2000). The particle size of liquid clouds needed for radiation calculations is diagnosed from the prognosed liquid water content and an assumed cloud droplet number concentration which is specified to be 300 cm^{-3} over land and 100 cm^{-3} over ocean. For ice clouds, the particle size is specified as a function of temperature based upon an analysis of aircraft observations (Donner et al. 1997). Clouds are assumed to randomly overlap. Because of the coarse vertical resolution in the upper troposphere (Table 2), this assumption is acceptable there, but for clouds in the lower troposphere this assumption is poor (Hogan and Illingworth 2000).

Cloud fraction is also treated as a prognostic variable of the model following the parame-

terization of Tiedtke (1993) with two important changes. The first change involves the treatment of super-saturated conditions in grid-cells. In these conditions, it is judged that the parameterization has omitted some missing condensation process. In Tiedtke (1993), any vapor in excess of supersaturation was condensed directly into precipitation without making cloud water. In AM2/LM2, this excess vapor is condensed into cloud instead of precipitation. This is justified because the AM2/LM2 implementation omits some key condensation terms, such as the boundary layer condensation source term from Tiedtke (1993).

The second change involves the erosion constant, a key unknown parameter in the Tiedtke parameterization, that governs the rate at which sub-grid scale mixing dissipates clouds in sub-saturated grid cells. Rather than use a single globally constant value (Tiedtke 1993), the erosion constant is made a function of the state of the grid cell in AM2/LM2. If vertical diffusion is acting in a grid cell, the erosion constant is set to the large value of $5 \times 10^{-5} \text{ s}^{-1}$ which ensures rapid dissolution of clouds in sub-saturated cells. If convection is occurring without vertical diffusion, the erosion constant is set to the smaller value of $4.7 \times 10^{-6} \text{ s}^{-1}$. If neither convection nor vertical diffusion is occurring in a grid cell, then the erosion constant is set to the even smaller value of $1 \times 10^{-6} \text{ s}^{-1}$, the original value used in Tiedtke (1993). The relative values of the erosion constant reflect the degree of sub-grid scale turbulence and mixing occurring in a grid cell. In fully turbulent layers, the mixing is rapid so that partially cloudy regimes should be more transitory (in the absence of sources of partial cloudiness) than in quiescent conditions for which partly cloudy conditions could exist for a long time. The erosion constant in the presence of convection is very influential in controlling the brightness of trade cumulus regions. However, the value of $4.7 \times 10^{-6} \text{ s}^{-1}$ used in the presence of convection is about 40 times smaller than the value for the erosion constant suggested by analysis of large-eddy simulations of trade cumuli from the Barbados

Oceanographic and Meteorological Experiment (BOMEX) (Siebesma et al. 2003). This may partly explain why the shortwave reflection from trade cumulus regions is too large (Figure 10, below).

The model's radiation budget is tuned so that the long-term global and annual mean outgoing longwave and absorbed solar radiation are close to observed and that the net radiative balance is between 0 and 1 W m⁻². This is accomplished primarily through adjustments to the cloud drop radius threshold value for the onset of raindrop formation (a value of 10.6 μm is used), the erosion constant in the presence of convection, and to the specified precipitation efficiency for deep convection in RAS. Although a critical radius of 10.6 μm is smaller than can be justified, it is considerably larger than values used previously in other large-scale models. The value used in AM2/LM2 is perhaps close enough to realistic values that the lack of sub-grid scale variability to cloud water in microphysical calculations may be the reason that large-scale models tune this parameter (Rotstayn 2000, Pincus and Klein 2000).

4) SURFACE FLUXES

Surface fluxes are computed using Monin-Obukhov similarity theory, given the atmospheric model's lowest level wind, temperature, and humidity and the surface roughness lengths, temperature, and humidity. To recognize the contribution to surface fluxes from sub-grid scale wind fluctuations, a 'gustiness' component proportional to the surface buoyancy flux is added to the wind speed used in the flux calculations (Beljaars 1995). Oceanic roughness lengths for momentum, heat, and moisture are prescribed according to Beljaars (1995). As a result of this prescription for roughness lengths, the exchange coefficients for momentum increase with wind speed whereas the heat and scalar exchange coefficients remain fairly constant across a wide

range of wind speed.

The treatment of surface fluxes in highly stable conditions requires special attention as with traditional formulations, the temperature of the surface will decouple from that of the atmosphere leading to excessive cooling of the winter land surface (Derbyshire 1999). In order to prevent this decoupling, the stability functions are modified so that mixing will occur for Richardson numbers greater than 0.2. This pragmatic fix for a problem common to many models will hopefully be replaced with a more physically based treatment based on the active research in this area (Holtslag 2003).

Recognizing that flow over hills with horizontal length scales smaller than those that generate gravity waves induces substantial drag on the atmosphere, a parameterization for ‘orographic roughness’ has been introduced (Wood and Mason 1993). In this parameterization, an ‘effective roughness’ length proportional to the standard deviation of orography at sub-grid scales is used to enhance the exchange coefficient for momentum. The exchange coefficients for heat and scalars are unaltered. In the absence of this parameterization, anomalous low level jets occurred in the vicinity of steep orography gradients.

5) TURBULENCE

Vertical diffusion coefficients are predicted according to their physical context. A K-profile scheme based upon Lock et al. (2000) is used for convective boundary layers and near-surface convective layers driven by strong longwave cooling from cloud tops (i.e. stratocumulus convection). The top of the convective boundary layer is determined by lifting a near surface parcel to its level of neutral buoyancy. Likewise, the bottom of the stratocumulus layer is determined by low-

ering a radiatively cooled parcel to its level of neutral buoyancy. For both types of convection, the mixing across the top of these layers is prescribed with an entrainment parameterization which is based upon a combination of observation and large eddy simulation results. For the convective boundary layer, the entrainment parameterization follows that of Lock et al. 2000 for which the entrainment rate is proportional both to the surface buoyancy flux and the surface wind stress and is inversely proportional to the strength of the inversion at the top of the convective layer. For stratocumulus layers, a parameterization for the entrainment rate w_e is used which approximately reduces to:

$$w_e = \frac{0.5\Delta F_{LW}}{\rho c_p \Delta \theta_{vl}} \quad (2)$$

where ΔF_{LW} is the longwave flux divergence across cloud top in W m^{-2} , c_p is the heat capacity of air at constant pressure, and $\Delta \theta_{vl}$ is the jump in liquid water virtual potential temperature across the entrainment interface. This parameterization differs from Lock et al. 2000 in that the buoyancy reversal term has been omitted which is justified as follows. To accurately calculate the buoyancy reversal term requires a good prediction of the liquid water content at cloud top. However, confidence in the model's prediction of cloud top liquid water is low because no provisions have been made to account for the sub-grid vertical structure of the inversion layer as is done in Lock (2001) and Grenier and Bretherton (2001). In the absence of the buoyancy reversal term, the radiatively driven entrainment rate has been enhanced by increasing the constant in (2) to 0.5, approximately double the value used in Lock et al. (2000).

For layers of the atmosphere which are not part of either a convective planetary boundary layer or a stratocumulus layer, a local mixing parameterization is used. For unstable layers, the

mixing coefficients of Louis (1979) are used. For stable turbulent layers, conventional stability functions for which mixing ceases when the Richardson number exceeds 0.2 are used except near the surface. If the surface layer is under stable conditions, the stability functions which provide enhanced surface fluxes for Richardson numbers in excess of 0.2 (section 2b4) are blended with the conventional stability functions in the lowest kilometer of the atmosphere. This is done to provide a smooth transition from enhanced mixing near the surface to conventional mixing aloft.

Finally, the vertical diffusion coefficients are given ‘memory’ by making the diffusion coefficients prognostic variables and damping their values to those diagnosed from the instantaneous state with a damping time scale of one hour. This treatment prevents a $2\Delta t$ oscillation in stable turbulent layers.

6) GRAVITY WAVE DRAG

Orographic gravity waves are parameterized according to Pierrehumbert (1986) and Stern and Pierrehumbert (1988). The momentum flux is a function of its surface value τ_s and the vertical profile of the saturation flux τ^* required for wave breaking. The surface flux τ_s is specified as:

$$\tau_s = - \frac{\rho U^3}{N\lambda} G(F) \quad (\text{for } N^2 > 0) \quad (3)$$

where U is the low level horizontal wind velocity, N is the low level Brunt-Vaisala frequency, and λ is an effective horizontal mountain wavelength with a fixed value of 100 km. G is a function of the Froude number F ($= Nh/U$, where h is the sub-grid scale mountain height) and is specified as:

$$G(F) = G^* \left(\frac{F^2}{F^2 + a^2} \right). \quad (4)$$

In AM2, the constants G^* and a have both been tuned to a value of 1 to optimize the simulation of zonal mean winds and sea level pressure gradients. The height dependent value of the saturation flux τ^* is given by:

$$\tau^* = -\rho U^2 D G^* / \lambda \quad (5)$$

where D is the vertical wavelength of the gravity waves determined from WKB theory. The flux at a given level is equal to the flux in the level immediately below or τ^* , whichever is smaller.

Note that this parameterization omits enhanced low level drag for high F and anisotropic effects (the stress at all levels is opposite the direction of the low level wind). The omission of enhanced low level drag is partly compensated by enhanced drag due to orographic roughness (Section 2b4).

c. Land model LM2

The land model LM2 is based on the Land Dynamics (LaD) model described in detail by Milly and Shmakin (2002; hereinafter MS02). At unglaciated land points, water may be stored in three lumped reservoirs: snow pack, soil water (representing the plant root zone), and ground water. Energy is stored as sensible heat in 18 soil layers and as latent heat of fusion in snow pack and all soil layers except the top layer. For simplicity the soil latent heat, which was neglected by MS02, is treated in an idealized fashion; every soil grid cell except the top layer is assumed to have 300 kg m^{-3} “freezable water” that is hydraulically isolated from the water cycle. For water

mass balance, soil water and ground water are not allowed to freeze, regardless of temperature. Evapotranspiration from soil is limited by a non-water-stressed bulk stomatal resistance and a soil-water-stress function. Drainage of soil water to groundwater occurs when the water capacity of the root zone is exceeded. Groundwater discharge to surface water is proportional to groundwater storage. Model parameters vary spatially as functions of mapped vegetation and soil types but are temporally invariant. Certain LaD-model parameter values were modified from those assigned by MS02 for coupling with AM2; these are described below.

Parameters affecting surface albedo (snow-free surface albedo, snow albedo, and snow-masking depth) were tuned on the basis of a comparison of model output with NASA Langley Surface Radiation Budget data analyses (Darnell et al. 1988, Gupta et al. 1992). Additionally, to improve albedo fields, three sparse-vegetation classes of Matthews (1983) were re-assigned relative to MS02 so that only the Matthews' 'desert' class remained as desert in LM2; the other three were re-defined as grassland. In another departure from MS02, the geographic variation of snow-free albedo of desert was prescribed on the basis of annual mean albedo from the Earth Radiation Budget Experiment (ERBE, Barkstrom et al. 1989). This was done because albedo of deserts has large regional variations; to represent all deserts with a single albedo, as is done for the other vegetation classes, was judged to produce unacceptably large errors.

When the LaD model was first run as LM2 coupled to AM2, computed values of evaporation from land were generally smaller than expected for the AM2 precipitation and surface net radiation. To remedy this bias, the non-water-stressed values of bulk stomatal resistance were reduced globally in LM2 by a factor of 5 from the values previously determined by stand-alone tuning of the LaD model (MS02). The magnitude of this reduction was chosen to produce rates of

evaporation having relations to precipitation and surface net radiation consistent with the semi-empirical relation of Budyko (1974). The necessity for such a large parameter adjustment was unexpected and is under investigation. Discrepancies between stand-alone and coupled tuning of the LaD model may be related to fundamental problems in the stand-alone tuning strategy, which does not permit atmospheric feedbacks.

The heat capacity of soil for soil depths less than 0.3 m was reduced globally by a factor of 4 so that the diurnal temperature range of near-surface air simulated by AM2/LM2 is generally consistent with the Climate Research Unit (CRU) observations of New et al. (1999). The need to adjust the heat capacity in order to increase the diurnal temperature range is understandable, because it compensates for systematic errors in the original model. In humid regions, the model assumption of an isothermal surface, in which the vegetation canopy and soil surface are at a common temperature, promotes excessive sensible heat flux into the ground. In arid regions, the model use of a global average soil wetness leads to overestimation of the soil heat capacity and thermal conductivity. The need for this adjustment is not surprising because MS02 focused on the long-term mean water and energy balances, quantities that are very insensitive to the soil heat capacity.

The vertical structure of the soil levels was changed from the MS02 values so that the total soil depth is 6 m with the thickness of soil levels changing from 0.02 m at the top to 1 m at the bottom. Relative to MS02, the thicker near-surface levels suppress numerical problems introduced when the near-surface heat capacity was reduced, and the deeper soil domain permits the full effect of seasonal heat storage to be realized.

d. Boundary conditions and integrations performed

The standard integration described in this study uses the observationally-based AMIP II SST and sea-ice prescriptions (Gates et al. 1999). The period of integration is from 1 January 1979 to 1 March 1996. The integration was initialized from another spun-up integration of the model with slightly different boundary conditions and forcing from the AMIP prescription. The model output from this integration was submitted to the PCMDI in February 2004. A monthly climatology was formed from this integration for the years 1979 through 1995 and was compared to observations in sections 3a and 4.

A second set of integrations discussed below is a 10-member ensemble of 50-year integrations, from January 1951 to December 2000, that uses another SST and sea-ice data prescription developed by J. Hurrell at NCAR (personal communication). The data from these integrations are used in the analysis of variability related to ENSO (sections 3b1 and 3b2) and the Northern Annual Mode (section 3b3).

3. Simulation characteristics

a. Model climatology

1) GENERAL CIRCULATION

Figure 1 shows the difference in annual- and zonal-mean temperature between the long-term mean of the AMIP II integration of AM2/LM2 and a 50-year climatology from the National Center for Environmental Prediction (NCEP) reanalysis (Kalnay et al. 1996). The model exhibits a cold troposphere and warm stratosphere bias throughout the year. Typical errors in seasonal

mean temperatures are 2 K and 4 K for tropospheric and stratospheric temperatures, respectively. The largest model bias occurs at the high latitudes of the Southern Hemisphere cold bias from 100 to 500 hPa. This bias is common to many climate models; however, the magnitude of the error in AM2/LM2 is smaller than in other models. Analyses from both NCEP and the European Centre for Medium Range Weather Forecasts (ECMWF, Gibson et al. 1997) indicate zonal mean 200 hPa December-January-February (DJF) temperatures of about 225-227 K at 60°S to 90°S, whereas AM2/LM2 gives temperatures of 219 K for this region. In contrast, the median AMIP II model has temperatures of about 211 K (P. Gleckler, personal communication). Reasons for this reduced cold bias of 200 hPa temperature are under investigation.

The tropospheric cold bias evident in Figure 1 extends to the land surface, as can be seen in the annual-mean 2 m air temperature bias with respect to the CRU climatology (Fig. 2). Although the annual-mean is fairly representative of the full seasonal cycle, warm biases do appear in some seasons in specific regions. Such biases are apparent, for example, in boreal winter over central and northwestern North America, and in boreal summer over the southern United States (Fig. 3). The latter bias corresponds to a mean temperature of 303 K or 30°C.

Figure 4 displays the annual and zonal-mean zonal winds from AM2/LM2, NCEP reanalysis, and the difference. As for temperature, the largest wind errors are concentrated in the top levels of the model. Typical error amplitudes throughout the seasonal cycle are 1-2 m s⁻¹ in the troposphere and 5-10 m s⁻¹ in the stratosphere. Biases that persist throughout the seasonal cycle include a westerly bias in the tropical middle troposphere and a tendency for the extratropical jets to have 1-2 m s⁻¹ errors that are westerly near 40° latitude and easterly near 60-80° latitude. These dipolar error patterns correspond to negative annular-mode type signatures in each hemisphere

(Thompson and Wallace 1998, Thompson and Wallace 2000).

Figure 4 suggests annular mode type errors continue to surface. Figure 5 displays the long-term annual- and zonal- mean zonal wind stress over the ocean for AM2/LM2 and three observational based datasets (see caption for details). Although the spread is large among the observational datasets, robust biases are apparent: the AM2/LM2 surface wind stress amplitude is approximately 30% too large in the subtropics and the extratropical pattern displays distinctly the annular-mode type equatorward shift, particularly in the Northern Hemisphere.

Figure 6 illustrates the long-term mean Northern Hemisphere DJF sea level pressure (SLP) for AM2/LM2, the NCEP reanalysis, and the difference. The equatorward shift of the Northern Hemisphere surface circulation evident in the annual-mean wind stress (Fig. 5) corresponds to a bias toward stronger than observed SLP gradients equatorward of 60°N, particularly in the North Atlantic. Other biases include a slightly stronger than observed Icelandic and Aleutian lows, and a high pressure bias of 8 to 10 hPa over the Eastern Hemisphere Arctic. This error pattern is accompanied by anomalous easterlies in northwest Russia, which appear through temperature advection by the mean flow, to contribute to the enhanced cold bias in that region (Fig. 2). This temperature advection signal, the Arctic high-pressure bias and the low pressure error pattern at lower latitudes are also signatures of annular-mode type anomalies (Thompson and Wallace 2000; section 3b4 and Fig. 17). Note that this bias pattern is common to many models (Fig. 2 of Walsh et al. 2002).

Figure 7 displays the departure from zonal mean of the 500 hPa DJF geopotential height, a useful metric of the model's ability to produce a realistic planetary wave pattern. Typical errors are on the order of 20 m, with the most prominent errors being an anomalously strong ridge cen-

tered over the North American Pacific coast and a weaker than observed negative-to-positive dipole over the Hudson-Bay-to-North-Atlantic sector. Consistent with the latter error, the 200 hPa zonal wind over the North Atlantic displays a jet axis that has insufficient southwest-northeast tilt (not shown).

2) PRECIPITATION, RADIATION, CLOUDS, AND WATER VAPOR

Figure 8 compares the annual mean climatological precipitation for the model to the observational climatology of Xie and Arkin (1997), also known as CMAP. Although the correlation coefficient is high, 0.9, the root mean square error, 0.85 mm d^{-1} , is about 40% of the spatial standard deviation of the field, 2 mm d^{-1} . The most prominent errors are deficits of precipitation to the west of the Maritime continent, in the South and tropical Atlantic convergence zones, and in the eastern Pacific ITCZ. Precipitation excesses occur in tropical Africa, the western Indian ocean, and the northwest tropical Pacific oceans. In the annual mean, there are faint signatures of a double ITCZ marked by excessive precipitation near 5°S in the eastern Pacific and Atlantic. Although this error is larger during the March-April-May season, we highlight it here because coupled ocean-atmosphere models using AM2/LM2 exhibit a much more severe double ITCZ.

AM2/LM2 simulates too much summertime precipitation in Siberia, Alaska, and Northern Canada with the model producing double the CMAP precipitation. The positive bias in summertime high latitude precipitation is also present in the annual mean and is common to many models (Fig. 13 of Walsh et al. 2002). However, on an annual mean basis there does not appear to be a bias in precipitation minus evaporation; outflows from rivers feeding the Arctic ocean are not systematically overestimated (not shown). The global mean precipitation is $\sim 0.15 \text{ mm d}^{-1}$ higher than the CMAP mean of 2.68 mm d^{-1} (Table 3).

Figures 9 and 10 compare the long-term annual mean outgoing longwave radiation (OLR) and net shortwave absorbed (SWAbs) from AM2/LM2 to the ERBE observations. Root mean square errors are about 8 W m^{-2} for OLR and 13 W m^{-2} for SWAbs. Over the tropical oceans, the error patterns, particularly for OLR, resemble those of the precipitation errors, suggesting that improvements in the simulation of precipitation would be accompanied by improvements in the radiation fields. An interesting exception to this is that OLR is overestimated over tropical land areas where there is not a systematic underestimate of precipitation (e.g. tropical Africa). For the shortwave radiation budget, the most prominent error is the overestimation of SWAbs in the coastal zones of the eastern subtropical oceans. Although the model is effective in creating stratocumulus clouds further offshore, there is a severe deficit of coastal stratocumulus. This may reflect the fact that not enough care has been taken with the representation of entrainment across the strong inversions at the top of the boundary layer (Lock 2001). Away from the coasts, in the trade cumulus regions of the subtropics, there is an overestimation of the reflected shortwave. This may partly indicate that the erosion constant in the presence of convection is too small (section 2b3) and/or that the use of random cloud overlap assumption is poor for these regions. Altogether the pattern of “dim-stratocumulus-bright-trades” is endemic to atmospheric models (Siebesma et al. 2004).

In the extratropics, a prominent overestimate of SWAbs of about $10\text{-}20 \text{ W m}^{-2}$ occurs at nearly all longitudes of the southern ocean at about 60°S . The error occurs in the open ocean areas adjacent to the sea ice margin and has lead to anomalously warm SSTs in a coupled model built with AM2/LM2. Through comparison to data from the International Satellite Cloud Climatology Project (ISCCP, Rossow and Schiffer 1999), this error appears to be due to an underestimate of midlevel topped clouds.

Although the model's radiation has been tuned to resemble the top of atmosphere (TOA) radiation budget, the surface radiation budget is somewhat independent. Both the estimates of the Global Energy and Water Experiment (GEWEX) (Stackhouse et al. 2004) and the Goddard Institute for Space Studies (GISS) (Zhang et al. 2003) indicate that the shortwave absorbed at the surface is about 5 W m^{-2} too low (Table 3). The low bias in net shortwave absorbed results from the excess shortwave cloud forcing, which is the difference between clear sky and all-sky or total shortwave fluxes. From earlier integrations of AM2/LM2 without the specified three dimensional monthly climatology of aerosols, the SWAbs at the SFC is reduced by 5 W m^{-2} while the longwave cooling of the surface is reduced by less than 1 W m^{-2} due to the presence of aerosols. With regard to the surface longwave budget, it appears that AM2/LM2 overestimates the longwave cooling by about 10 W m^{-2} , although under clear skies there is less bias.

With regard to the turbulent surface fluxes, the model overestimates the Kiehl and Trenberth (1997) estimate of evaporation by about 5 W m^{-2} and underestimates the sensible heat flux by a similar amount. Note that the sum of the Kiehl and Trenberth (1997) turbulent heat fluxes, 102 W m^{-2} , is lower than the either the GEWEX or GISS estimates of the surface net radiation, about 115 W m^{-2} , by 10 to 15 W m^{-2} . Given the significant remaining uncertainties in the surface energy budget, the biases in the model's global mean turbulent heat fluxes are not well defined. Indeed the model's values lie within the range of observational estimates quoted in Table 1 of Kiehl and Trenberth (1997).

Figure 11 compares AM2/LM2's annual mean total cloud amount to the satellites estimates of ISCCP. The data used is the D2 adjusted monthly mean total cloud amounts (Rossow and Schiffer 1999). (A more thorough comparison of AM2/LM2 clouds to ISCCP data using an

‘ISCCP Simulator’ (Klein and Jakob 1999, Webb et al. 2001) will be reported elsewhere). AM2/LM2 does not produce enough clouds over oceans between 20° and 40° latitude, particularly in the coastal stratocumulus zone. Quantitatively, the model has a root-mean square error of 0.1 relative to both ISCCP and the surface observer climatology of Warren et al. (1986, 1988) (not shown). The globally averaged cloud cover of AM2/LM2 of 0.66 lies in between the ISCCP D2 value of 0.69 and the surface observers’ value of 0.62. Another noticeable problem of the model is the excessive wintertime cloudiness in northern Eurasia and North America; surface observers indicate about 0.5 cloud cover in these regions whereas AM2/LM2 has cloud cover in excess of 0.8. Much of this difference occurs in low cloudiness where the model has over 0.7 low cloudiness but the surface observers report low cloudiness under 0.3 (not shown). Averaged over the oceans, AM2/LM2’s liquid water path of 77 g m^{-2} is comparable to the two satellite estimates (Table 3) (Greenwald et al. 1993; Weng et al. 1997); however, this is achieved by an excess of liquid water path over midlatitude storm tracks and a deficit over tropical and subtropical oceans (not shown). The model’s simulation of ice water path cannot be assessed due to the lack of a reliable observational product with global coverage.

At the top of atmosphere, the magnitude of the global and annual averaged shortwave cloud forcing is overestimated by about 5 W m^{-2} but the longwave cloud forcing is underestimated by about 5 W m^{-2} (Table 3). Because the total OLR has been tuned to match ERBE observations, the underestimate of the longwave cloud forcing indicates a similar significant error in the clear-sky OLR. Although the clear-sky sampling bias may contribute a few W m^{-2} to this difference (Hartmann and Doelling 1991), the model’s clear-sky OLR is probably too low for two reasons. First, the troposphere has a cold bias relative to re-analyses (Fig. 1). Second, as shown in Figure 12, the model has a moist bias in the upper troposphere in comparison to estimates of upper trop-

ospheric (\sim 200-500 hPa) relative humidities from the TIROS Operational Vertical Sounder (TOVS) (Soden and Bretherton 1993). This moist bias is in excess of that due to the clear-sky sampling bias of the observations. This moist bias deduced from satellite observations is confirmed by both ECMWF and NCEP reanalyses which indicate a moist bias in both relative and absolute humidity in the middle tropical troposphere (not shown). The model's column water vapor (Table 3), a measure primarily of lower tropospheric water vapor, is slightly low, partially reflecting the model's cold bias.

b. Model variability

1) TROPICAL PRECIPITATION PATTERN ASSOCIATED WITH ENSO

The El Niño/Southern Oscillation (ENSO) is one of the most important contributors to atmospheric variability on interannual time scales. The ENSO related tropical precipitation anomalies represent a redistribution of diabatic heat sources and sinks that strongly influence the global atmospheric circulation. The response of AM2/LM2 to the prescribed ENSO-related SST anomalies are depicted in Figure 13, which shows the distribution of regression coefficients of precipitation rate on the standardized NINO3 index. The NINO3 index is defined as the areally averaged SST anomaly in the region 5°S - 5°N , 150°W - 90°W , and is a commonly used indicator of the amplitude and polarity of ENSO events. These coefficients have been multiplied by one standard deviation of the NINO3 index; thus they represent typical precipitation anomalies that accompany a one standard deviation increase in the NINO3 index. The upper panel of Figure 13 is based on the ensemble average of the 10 AM2/LM2 runs for the DJF season in the 1951-2000 period (section 2d), and the lower panel is computed using Global Precipitation Climatology Project (GPCP) data (Huffman et al. 1997) for 1979-2000.

The simulated precipitation signals during ENSO are generally in good agreement with the observations, as inferred from the GPCP dataset and from station measurements (Ropelewski and Halpert 1987). Both panels of Figure 13 indicate that warm ENSO events are associated with positive precipitation anomalies across much of the equatorial Pacific, and negative anomalies over equatorial South America and the neighboring Atlantic waters, as well as the northwestern and southwestern subtropical Pacific. One discrepancy between model and observation is seen along the equator over the eastern Indonesian Archipelago. The GPCP pattern shows negative rainfall anomalies in that region during warm events, whereas the model result portrays near-normal conditions.

2) EXTRATROPICAL TELECONNECTIONS TO ENSO

The impact of ENSO-related SST anomalies on the extratropical circulation is illustrated in Figure 14, which displays the regression coefficients of 200 hPa height on the standardized NINO3 SST index for the DJF season. These charts have been constructed using NCEP reanalysis data (lower panels) and the ensemble average of the 10 AM2/LM2 integrations (upper panels). In analogy with Figure 13, the regression statistics in Figure 14 portray the typical 200 hPa height anomalies in response to a one-standard deviation SST forcing from the tropical Pacific. Similar charts have been presented by Horel and Wallace (1981), among many others, to illustrate the relationship between ENSO and the extratropical flow pattern.

The comparison between the upper and lower panels in this figure reveals considerable spatial similarities between the simulated and observed wavetrains emanating from the NINO3 region to the eastern North Pacific/North American sector and the Southern Oceans. The overall resemblance between the teleconnection patterns derived from the model output and re-analysis

data is attributable to the realistic simulation of the tropical precipitation forcing associated with ENSO (Fig. 13). A noticeable error is that AM2/LM2 underestimates the magnitude of the model anomaly over Canada.

The capability of the model to reproduce the Northern Hemisphere circulation anomalies observed in individual El Niño and La Niña events is now examined. For each of the prominent warm and cold events in the 1951-2000 period (e.g., see listing in Trenberth 1997), the anomaly patterns of DJF 200 hPa height were computed using the NCEP reanalysis and the ensemble mean of the 10 model integrations. The spatial correlation coefficient, root mean square (rms) difference, and ratio between the spatial variances of the model and observed fields in the North Pacific/North American sector (20° - 70° N, 60° - 180° W) are displayed using a ‘Taylor’ diagram (Gates et al. 1999 and Taylor 2001) in Figure 15. In this diagram, each event is indicated by a dot and a label corresponding to the last two digits of the year; for instance, the statistics for the 1982/83 El Niño event are indicated using the label ‘82’. The spatial correlation coefficient between the simulated and observed anomalies is at the 0.5 level or greater for four (1969, 1982, 1991 and 1997) out of the eight warm events, and all seven cold events. While the spatial variance of the ensemble mean model pattern is noticeably lower than that of the observations, inspection of the Taylor diagram for the ten individual members of the ensemble (not shown) reveals that the spatial variance of these members is in better agreement with the observations. The Taylor diagram for individual samples further illustrates that, for those events with high spatial correlation between the ensemble-mean and observations (e.g. 1982 and 1997), the agreement between many model samples and the observations is also high.

3) ENSO - MONSOON RELATIONSHIPS

Ample observational and model evidence exists for the impact of ENSO on the Asian-Australian monsoons; e.g., see the brief review of pertinent studies by Lau and Nath (2000). Warm ENSO episodes are generally accompanied by below normal precipitation during the wet summer monsoons over the Indian subcontinent (IND) and northern Australia (AUS). Additionally, the dry winter monsoon over southeast Asia (SEA) weakens in El Niño events resulting in above average rainfall amounts. The polarity of these anomalies tends to reverse during cold events.

The simulation of these ENSO-monsoon relationships by AM2/LM2 has been evaluated by examining the model's 10-member ensemble mean precipitation anomalies in the above-mentioned regions for each monsoon season in the 1951-2000 period. The relationship between the model's precipitation anomalies in these monsoon regions and the NINO3 SST anomalies is illustrated in the upper panels of Figure 16. The simulated precipitation anomalies in IND and AUS during the local summer season are negatively correlated with NINO3 SST anomalies, and the wintertime rainfall in SEA exhibits a positive correlation with the ENSO forcing. Many of the outstanding ENSO episodes (colored dots and squares) are accompanied by notable simulated rainfall perturbations simulated in the regions considered. The correlation coefficients between monsoon precipitation amounts in the AM2/LM2 model runs and the NINO3 index, as indicated in the upper right corner of individual panels, may be compared with those deduced from GPCP observational estimates (lower panels of Fig. 16). The noticeably weaker correlations between the observed Indian rainfall and the NINO3 index (lower left panel) reflect the much diminished Indian monsoon - ENSO relationships during the recent decades covered by the GPCP dataset (Kumar et al. 1999). The correlation coefficients between the observed rainfall anomalies and the

NINO3 index for the outstanding ENSO episodes (shown above the lower panels without parenthesis) are based on only five events, and are hence subject to considerable sampling fluctuations.

4) NORTHERN ANNULAR MODE

Apart from ENSO, the dominant pattern of interannual climate variability is associated with the annular modes of the extratropical atmospheric circulation field. Shown in Figure 17 are distributions of sea level pressure (SLP) and surface temperature anomalies associated with the Northern Annular Mode (NAM, also referred to as the Arctic Oscillation; see Thompson and Wallace (1998, 2000)) for the observations and AM2/LM2. The NAM is defined as the first empirical orthogonal function (EOF) of sea level pressure over the domain from 20°N to 90°N. The contours indicate the sea level pressure changes associated with a 1 hPa increase of a NAM index. The NAM index is defined as the difference in sea level pressure between the Arctic and midlatitude extrema of the EOF pattern, multiplied by the EOF time series, thereby giving an index with units of hPa.

The model has a highly realistic simulation of the spatial pattern of the NAM. The color shading indicates the near-surface air temperature anomalies associated with a 1 hPa increase in the NAM index. The AM2/LM2 NAM pattern shown is the mean of NAM patterns computed separately for each of the 10 ensemble members integrated with observed SSTs from 1951 to 2000. Examination of the NAM pattern from each of the 10 members of the ensemble reveals relatively small intra-ensemble variations in the spatial pattern of the NAM. Consistent with the observations, a positive phase of the simulated NAM is associated with a quadrupole field of temperature anomalies: warm anomalies over southeastern North America and northern Eurasia and negative anomalies over northeastern North America and northern Africa through the Middle East. The

primary discrepancy between the simulated and observed temperature anomalies occurs over northwestern North America, with larger negative temperature anomalies in AM2/LM2 than observed. This is consistent with Northeast Pacific SLP gradients that are stronger than observed.

5) TROPICAL TRANSIENT ACTIVITY

Transient activity in the tropics is evaluated by examination of 2 phenomena: tropical cyclones and the Madden-Julian Oscillation (MJO, Madden and Julian 1972).

Tropical cyclones in AM2/LM2 are detected using the algorithm of Vitart et al. (1997) and compared to the National Climate Data Center's global tropical cyclone data set (Neumann et al. 1999). Figure 18 displays genesis location frequencies for the years 1979-1995. AM2/LM2 underestimates the number of storms quite significantly, particularly in the North Atlantic and the Eastern Pacific, where no storms occur. The seasonal cycle in the Northern Hemisphere (not shown) is also quite poor, with the model lagging observations by several months. Overall AM2/LM2's simulation of tropical cyclones is inferior to that of some other models (Bengtsson et al. 1995; Vitart and Stockdale 2001).

An assessment of the MJO is made by examining the structure and behaviour of intraseasonal variability (ISV), defined here as variability with timescales between 30 and 90 days. Figure 19 displays the wave frequency spectra, with the annual cycle removed, for deviations of the 200 hPa zonal wind from its zonal mean. Pentad data from January through December, averaged between 5°S and 5°N, from 1979 through 1995 were used to compute spectra for each year. These spectra were then averaged over the 17 years and smoothed further by the application of a 3-point Hanning window. A broad peak in the intraseasonal range is evident in the spectra for the NCEP

reanalyses, with the observed maxima primarily in the 40 to 60 day range. AM2/LM2 shows weaker peaks in the vicinity of 35 and 50 days with additional power at periods around 90 days, implying a somewhat slower propagation speed. In addition, a stronger preference for eastward propagation is seen in the NCEP reanalyses than in AM2/LM2. MJO structure and propagation characteristics may be studied by applying extended empirical orthogonal function analysis (EOF) to precipitation in the region 30°S - 30°N and 30°E - 90°W. To focus on MJO timescales the data is band-passed (30 to 90 day) and the EOF analysis is performed using lags from -7 to +7 pentads (-35 to + 35 days). Composite MJO life cycles are obtained by using peaks in the EOF mode-1 time series to identify centers of events. Then each event is taken to be -7 pentads to +7 pentads relative to these mid-points and all thus identified events are averaged together. Figure 20 shows a comparison of MJO composite life cycles, during November to April, from the AM2/LM2 on the left and the CMAP observed precipitation on the right. The months from November to April were selected as the MJO is most active then. Each panel in the figure represents an average of 3 adjacent time lags. The CMAP observations display coherent intraseasonal activity in the central and eastern Indian Ocean which propagates eastward across the maritime continent into the western Pacific. (The green dashed lines in Figure 20 indicate the propagation of the anomalies) AM2/LM2 shows weaker, less coherent activity with perhaps some slower eastward propagation from the maritime continent into the western Pacific. (Note that the AM2/LM2 anomalies have been multiplied by 2 for display in Figure 20) AM2/LM2 is particularly deficient in the Indian Ocean south of the Bay of Bengal when compared to CMAP. Waliser et al. 2003, indicate that this is a common deficiency of large-scale models. Overall, AM2/LM2's simulation of the MJO is fairly poor.

4. Comparison of AM2/LM2 climatology to other models

It is of general interest to compare the capability of AM2/LM2 to reproduce observed climate with that of other models. To do so, Taylor diagrams (see legend of Figure 15 for a detailed explanation of these diagrams) have been calculated for eight variables using AM2/LM2, two previous GFDL models, and four non-GFDL models (Fig. 21). The first row of Figure 21 displays variables associated with surface climate, including boreal winter ocean-only SLP, boreal summer Northern Hemisphere land-only surface air temperatures, and annual mean ocean-only zonal wind stress. The second row displays variables related to hydrology: annual mean tropical precipitation, shortwave cloud forcing, and total cloud amount. The last row displays variables related to upper tropospheric circulation: the boreal winter 200 hPa eddy geopotential in the Northern Hemisphere and the 200 hPa zonal wind.

The previous GFDL models include the GFDL climate model recoded into FMS software which is known locally as the Manabe Climate Model (MCM) (Delworth et al. 2002) and the model developed by the GFDL's former experimental prediction group (DERF) (Stern and Miyakoda 1995). The data from models outside of GFDL were acquired from the archive maintained at the PCMDI and represents their official submission to AMIP II. The outside models include the CCM3.5 of the National Center for Atmospheric Research, ECHAM4 of the Max Planck Institute, the ECMWF model CY18R5, and HadAM3 from the United Kingdom's Meteorological Office. The experimental data produced by the non-GFDL models were submitted to PCMDI in either 1998 or 1999 (see <http://www-pcmdi.llnl.gov/amip/STATUS/incoming.html> for documentation).

Broadly speaking, Figure 21 indicates that AM2/LM2 produces a model climate better than those of the previous GFDL models. The quality of AM2/LM2's climate is comparable to that produced by the non-GFDL models. In some variables (SLP, wind stress, 200 hPa circulation and precipitation), the AM2/LM2 model is at the front rank, but for shortwave cloud forcing AM2/LM2 is slightly worse. It is important to state three caveats of this model comparison: these Taylor diagrams compare only model climatologies with no results shown for different aspects of model variability; the performance of non-GFDL models may have improved in the years since their submission of data to AMIP II; and the Taylor diagrams are based on large scale patterns and do not assess important regional biases.

5. Future work

A new global atmosphere and land model AM2/LM2 developed at GFDL has been presented and the model evaluated using simulations in which the model is forced with observed SSTs and sea ice. In this final section, the suitability of AM2/LM2 for coupling with an ocean model and future plans for global atmosphere and land modeling at GFDL are discussed.

An important goal for this work is to couple AM2/LM2 to an ocean model without flux adjustments. This has been accomplished and will be reported elsewhere. Here, a preliminary indication of the ability of AM2/LM2 to couple with an ocean model is given by estimates of the implied poleward oceanic heat transport for the Atlantic, Indo-Pacific, and world ocean basins (Fig. 22). For comparison, observation based estimates of oceanic heat transport derived from atmospheric data (Trenberth and Caron 2001) and oceanic data (Ganachaud and Wunsch 2003) are also shown. AM2/LM2's implied oceanic heat transport is in reasonable agreement with the

GFDL GAMDT

observed estimates in the Atlantic basin, although it is typically near the low end of the confidence intervals reported for the observed estimates, and in a few cases, such as the Ganachaud and Wunsch estimates for 24°N and 19°S, the model lies outside the confidence intervals on the low side. In the North Atlantic, AM2/LM2's simulation of about 1 petawatt (10^{15} W) at 10°N-30°N represents a significant improvement over that implied by the atmospheric component of the older GFDL R30 climate model (Delworth et al. 2002), which had too small implied poleward heat transport (0.7 petawatts at 15°N, not shown). In the Indo-Pacific basin, the model's implied oceanic heat transport has a positive bias relative to both sets of observed estimates, and exceeds Trenberth and Caron's 1 standard error limit over all latitudes. This positive bias for the Indo-Pacific is reflected in a similar but less pronounced bias for the world ocean basin. These results indicate that in the North Pacific AM2/LM2 removes heat from the ocean at a greater rate than is supported by either set of observations. This difference from observations likely contributes to a large cold bias in the North Pacific when AM2/LM2 is coupled to an ocean model (details to be reported elsewhere).

The development of the next version of the atmospheric model, AM3, is well under way with a number of changes being explored and evaluated through the model development process. These include:

- Replacement of the B-grid dynamical core with a finite volume dynamical core (Lin 2004).
- Replacement of RAS with a convection scheme which includes representations of vertical velocities and microphysics in cumulus updrafts and downdrafts, and parameterized mesoscale circulations (Donner et al. 2001).

- Replacement of random cloud overlap with by a resolution invariant overlap scheme. This will be accomplished by a stochastic treatment of clouds (Pincus et al. 2003). Also under consideration is the replacement of the prognostic cloud fraction scheme (Tiedtke 1993) with a statistical cloud scheme with prognostic higher order moments similar to Tompkins (2002).
- Addition of more vertical levels at the top of the model to better simulate the stratosphere and its coupling with the troposphere. Consideration is being given to a new anisotropic orographic gravity wave scheme (Garner 2003) and to a convectively generated gravity wave scheme (Alexander and Dunkerton 1999).
- Addition of prognostic chemistry and aerosol modules based on the chemistry scheme developed for use in the MOZART-2 chemical transport model (Horowitz et al. 2003).
- Replacement of LM2 with a new dynamic land surface model with carbon and vegetation dynamics. This new land model, LM3, includes the various processes that determine the amount of carbon stored in the soil and the vegetation. These processes include changes in CO₂ concentrations and other environmental factors, natural disturbances (e.g. fire), and anthropogenic land use (e.g. deforestation and agricultural crop-land abandonment).

Acknowledgments. Former GFDL director Jerry Mahlman is thanked for his encouragement and support of the Flexible Modeling System and current GFDL director Ants Leetmaa is thanked for his chartering of the Global Atmospheric Model Development Team. Reviews of the manuscript by Olivier Pauluis, Mike Winton and two anonymous reviewers are appreciated. Assistance regarding surface radiation budget data provided by Paul Stackhouse and Yuanchong Zhang is appreciated.

References

- Alexander, M.J. and T.J. Dunkerton, 1999: A spectral parameterization of mean-flow forcing due to breaking gravity waves. *J. Atmos. Sci.*, **56**, 4167-4182.
- Arakawa, A. and V. R. Lamb, 1977: Computational design of the basic dynamical processes of the UCLA general circulation model. *Methods in Computational Physics*, Vol. 17, J. Chang, Ed., Academic Press, 173-265.
- Barkstrom, B. R., E. Harrison, G. Smith, R. Green, J. Kibler, R. Cess, and the ERBE Science Team, 1989: Earth Radiation Budget Experiment (ERBE) archival and April 1985 results. *Bull. Amer. Met. Soc.*, **70**, 1254-1262.
- Beljaars, A. C. M., 1995: The parameterization of surface-fluxes in large-scale models under free convection. *Quart. J. Roy. Meteor. Soc.*, **121**, 255-270.
- Beljaars, A. C. M., 1998: Role of the boundary layer in a numerical weather prediction model, in Clear and Cloudy Boundary Layers, A. A. M. Holtslag, P. G. Duynkerke, and P. J. Jonker, Eds., Royal Netherlands Academy of Arts and Sciences, 287-304.
- Bengtsson, L., M. Botzet and M. Esch, 1995: Hurricane-type vortices in a general circulation model. *Tellus*, **47A**, 175-196.
- Budyko, M. I., 1974: Climate and Life. Academic, 508 pp.
- Cahalan, R. F., W. Ridgway, W. J. Wiscombe, T. L. Bell, and J. B. Snider, 1994: The albedo of fractal stratocumulus clouds. *J. Atmos. Sci.*, **51**, 2434-2460.

GFDL GAMDT

CERSAT-IFREMER, 2002: Mean Wind Fields (MWF product), User manual. Volume 1: ERS-1, ERS-2, and NSCAT. C2-MUT-W-05-IF. Brest, France, 72 pp. (available at ftp://ftp.ifremer.fr/ifremer/cersat/documentation/gridded/mwf-ers/mwf_vol1.pdf)

Clough, S. A., M. J. Iacono and J-L. Moncet, 1992: Line-by-line calculations of atmospheric fluxes and cooling rates: Application to water vapor. *J. Geophys. Res.*, **97**, 15761-15785

Colella, P. and P. R. Woodward, 1984: The piecewise parabolic method (PPM) for gas-dynamical simulations. *J. Comput. Phys.*, **54**, 174-201.

Darnell, W. L., W. F. Staylor, S. K. Gupta, and F. M. Denn, 1988: Estimation of surface insolation using sun-synchronous satellite data. *J. Clim.*, **1**, 820-836.

A. daSilva, A. C. Young, and S. Levitus, 1994. Atlas of surface marine data 1994. Volume 1: Algorithms and procedures. Technical Report #6, U.S. Department of Commerce, NOAA, NESDIS, 1994.

Delworth, T. L., R. J. Stouffer, K. W. Dixon, M. J. Spelman, T. R. Knutson, A. J. Broccoli, P. J. Kushner, and R. T. Wetherald, 2002: Review of simulations of climate variability and change with the GFDL R30 coupled climate model. *Clim. Dyn.*, **19**, 555-574.

Derbyshire, S. H., 1999: Boundary-layer decoupling over cold surfaces as a physical boundary instability. *Bound.-Layer Meteor.*, **90**, 297-325.

Donner, L. J., C. J. Seman, B. J. Soden, R. S. Hemler, J. C. Warren, J. Strom, and K.-N. Liou, 1997: Large-scale ice clouds in the GFDL SKYHI general circulation model. *J. Geophys. Res.*, **102**, 21745-21768.

GFDL GAMDT

- Donner, L. J., C. J. Seman, R. S. Hemler, and S. Fan, 2001: A cumulus parameterization including mass fluxes, convective vertical velocities, and mesoscale effects: thermodynamic and hydrological aspects in a general circulation model. *J. Clim.*, **14**, 3444-3463.
- Edwards, J. M. and A. Slingo, 1996: Studies with a flexible new radiation code. I: Choosing a configuration for a large-scale model. *Quart. J. Roy. Meteor. Soc.*, **122**, 689-719.
- Fortuin, P. and H. Kelder, 1998: An ozone climatology based on ozonesonde and satellite measurements. *J. Geophys. Res.*, **103**, 31709-31734.
- Freidenreich, S. M., and V. Ramaswamy, 1999: A new multiple-band solar radiative parameterization for general circulation models. *J. Geophys. Res.*, **104**, 31389-31409.
- Fu, Q. and K.N. Liou, 1993: Parameterization of the radiative properties of cirrus clouds. *J. Atmos. Sci.*, **50**, 2008-2025.
- Gadd, A. J., 1978: A split explicit integration scheme for numerical weather prediction. *Quart. J. Roy. Meteor. Soc.*, **104**, 569-582.
- Ganachaud, A. and C. Wunsch, 2003: Large-scale ocean heat and freshwater transports during the World Ocean Circulation Experiment. *J. Clim.*, **16**, 696-705.
- Garner, S. T., 2003: A topographic drag closure with analytical base flux. Preprints to the 14th annual conference on Atmospheric and Oceanic Fluid Dynamics, San Antonio, American Meteorological Society, 120-124.
- Gates, W.L., and Coauthors, 1999: An overview of the results of the Atmospheric Model Inter-

comparison Project (AMIP I). *Bull. Amer. Met. Soc.*, **80**, 29-55.

Gibson, J. K., P. Kallberg, S. Uppala, A. Hernandez, A. Nomura, and E. Serrano, 1997: ERA description. ECMWF Reanalysis Project Rep. Series 1, European Centre for Medium-Range Weather Forecasts, Reading, United Kingdom, 66 pp.

Gregory, D., R. Kershaw, and P. M. Innes, 1997: Parameterization of momentum transport by convection. II: Tests in single-column and general circulation models. *Quart. J. Roy. Meteor. Soc.*, **123**, 1153-1183.

Grenier, H. and C. S. Bretherton, 2001: A moist PBL parameterization for large-scale models and its application to subtropical cloud-topped marine boundary layers. *Mon. Wea. Rev.*, **129**, 357-377.

Greenwald, T. J., G. L. Stephens, and T. H. Vonder Haar, 1993: A physical retrieval of cloud liquid water over the global oceans using Special Sensor Microwave/Imager (SSM/I) observations. *J. Geophys. Res.*, **98**, 18,471-18,488.

Gupta, S. K., W. L. Darnell, and A. C. Wilber, 1992: A parameterization for longwave surface radiation from satellite data: Recent improvements. *J. Appl. Met.*, **31**, 1361-1367.

Gupta, S. K., N. A. Ritchey, A. C. Wilber, C. H. Whitlock, G. G. Gibson, and P. W. Stackhouse Jr., 1999: A climatology of surface radiation budget derived from satellite data. *J. Clim.*, **12**, 2691-2710.

Hamilton, K. P., R. J. Wilson, J. D. Mahlman, and L. Umscheid, 1995: Climatology of the SKYHI troposphere-stratosphere-mesosphere general circulation model. *J. Atmos. Sci.*, **52**, 5-43.

GFDL GAMDT

- Harrison, E. F., P. Minnis, B. R. Barkstrom, V. Ramanathan, R. C. Cess, and G. G. Gibson, 1990: Seasonal variation of cloud radiative forcing derived from the Earth Radiation Budget Experiment. *J. Geophys. Res.*, **95**, 18,687-18,703.
- Hartmann, D. L. and D. Doelling, 1991: On the net radiative effect of clouds. *J. Geophys. Res.*, **96**, 869-891.
- Haywood, J. M., V. Ramaswamy, and B. J. Soden, 1999: Tropospheric aerosol climate forcing in clear-sky satellite observations over the oceans. *Science*, **283**, 1299-1303.
- Held, I., R. S. Hemler and V. Ramaswamy, 1993: Radiative-convective equilibrium with explicit two-dimensional moist convection. *J. Atmos. Sci.*, **50**, 3909-3927.
- Hogan, R. J. and A. J. Illingworth, 2000: Deriving cloud overlap statistics from radar. *Quart. J. Roy. Meteor. Soc.*, **126**, 2903-2909.
- Horel, J. D. and J. M. Wallace, 1981: Planetary-scale atmospheric phenomena associated with the Southern Oscillation. *Mon. Wea. Rev.*, **109**, 813-829.
- Holtslag, A. A. M., 2003: GABLS initiates intercomparison for stable boundary layer case. GEWEX News, **13** (2), 7-8.
- Horowitz, L. W., S. Walters, D. L. Mauzerall, L. K. Emmons, P. J. Rasch, C. Granier, X. X. Tie, J.-F. Lamarque, M. G. Schultz, G. S. Tyndall, J. J. Orlando, and G. P. Brasseur, 2003: A global simulation of tropospheric ozone and related tracers: Description and evaluation of MOZART, version 2. *J. Geophys. Res.*, **108**, 4784, doi:10.1029/2002JD002853.

GFDL GAMDT

- Huffman, G. J., R. F. Adler, P. Arkin, A. Chang, R. Ferraro, A. Gruber, J. Janowiak, A. McNab, B. Rudolf, and U. Schneider, 1997: The Global Precipitation Climatology Project (GPCP) combined precipitation dataset. *Bull. Amer. Met. Soc.*, **78**, 5-20.
- Jakob, C. and S. A. Klein, 2000: A parameterization of the effects of cloud and precipitation overlap for use in general circulation models. *Quart. J. Roy. Meteor. Soc.*, **126**, 2525-2544.
- Jones, P. D., 1994: Hemispheric surface air temperature variations: a reanalysis and an update to 1993. *J. Clim.*, **7**, 1794-1802.
- Kalnay, E., and Coauthors, 1996: The NCEP/NCAR 40-year Reanalysis Project. *Bull. Amer. Met. Soc.*, **77**, 437-471.
- Kershaw, R., A. L. M. Grant, S. H. Derbyshire, and S. Cusack, 2000: The numerical stability of a parameterization of convective momentum transport. *Quart. J. Roy. Meteor. Soc.*, **126**, 2981-2984.
- Kiehl, J. T. and K. E. Trenberth, 1997: Earth's annual global mean energy budget. *Bull. Amer. Met. Soc.*, **78**, 197-208.
- Klein, S. A., and C. Jakob, 1999: Validation and sensitivities of frontal clouds simulated by the ECMWF model. *Mon. Wea. Rev.*, **127**, 2514-2531.
- Kumar, K. K., B. Rajagopalan, and M. A. Cane, 1999: On the weakening relationship between Indian monsoon and ENSO. *Science*, **284**, 2156-2159.
- Kurihara, Y. and G. J. Tripoli, 1976: An iterative time integration scheme designed to preserve a

low-frequency wave. *Mon. Wea. Rev.*, **104**, 761-764.

Lau, N.-C., and M.J. Nath, 2000: Impact of ENSO on the variability of the Asian-Australian monsoons as simulated in GCM experiments. *J. Clim.*, **13**, 4287-4309.

Lin, S.-J., W. C. Chao, Y. C. Sud, and G. K. Walker, 1994: A class of the van Leer-type transport schemes and its application to the moisture transport in a general circulation model. *Mon. Wea. Rev.*, **122**, 1575-1593.

Lin, S.-J., 1997: A finite-volume integration method for computing pressure-gradient force in general vertical coordinates. *Quart. J. Roy. Meteor. Soc.*, **123**, 1749-1762.

Lin, S.-J., 2004: A “vertically Lagrangian” finite-volume dynamical core for global models. submitted to *Mon. Wea. Rev.*

Lindberg, C. and A. J. Broccoli, 1996: Representation of topography in spectral climate models and its effect on simulated precipitation. *J. Clim.*, **9**, 2641-2659.

Lock, A. P., A. R. Brown, M. R. Bush, G. M. Martin, and R. N. B. Smith, 2000: A new boundary layer mixing scheme. Part I: Scheme description and single-column model tests. *Mon. Wea. Rev.*, **128**, 3187-3199.

Lock, A. P., 2001: The numerical representation of entrainment in parameterizaions of boundary layer turbulent mixing. *Mon. Wea. Rev.*, **129**, 1148-1163.

Lord, S. J. and A. Arakawa, 1980: Interaction of a cumulus cloud ensemble with the large-scale environment. Part II. *J. Atmos. Sci.*, **37**, 2677-2692.

GFDL GAMDT

Louis, J.-F., 1979: A parameteric model of vertical eddy fluxes in the atmosphere. *Bound.-Layer Meteor.*, **17**, 187-202.

Madden, R. A. and P. R. Julian, 1972: Description of global-scale circulation cells in the tropics with a 40-50 day period. *J. Atmos. Sci.*, **29**, 1109-1123.

Mapes, B. E. and X. Wu, 2001: Convective eddy momentum tendencies in long cloud-resolving model simulations. *J. Atmos. Sci.*, **58**, 517-526.

Matthews, E., 1983: Global vegetation and land use: new high-resolution data bases for climate studies. *J. Appl. Met.*, **22**, 474-487.

Mellor, G.L. and T. Yamada, 1982: Development of a turbulent closure model for geophysical fluid problems. *Rev. Geophys. Space Phys.*, **20**, 851-875.

Mesinger, F., 1977: Forward-backward scheme, and its use in a limited area model. *Contrib. Atmos. Phys.*, **50**, 186-199.

Mesinger, F., Z. I. Janjic, S. Nickovic, D. Gavrilov and D. G. Deaven, 1988: The step-mountain coordinate: Model description and performance for cases of Alpine lee cyclogenesis and for a case of an Appalachian redevelopment. *Mon. Wea. Rev.*, **116**, 1493-1518.

Milly, P. C. D., and A. B. Shmakin, 2002: Global modeling of land water and energy balances. Part I: The land dynamics (LaD) model. *J. Hydrometeor.*, **3**, 283-299.

Moorthi, S. and M. J. Suarez, 1992: Relaxed Arakawa-Schubert: a parameterization of moist convection for general circulation models. *Mon. Wea. Rev.*, **120**, 978-1002.

GFDL GAMDT

Moorthi, S. and M. J. Suarez, 1999: Documentation of version 2 of Relaxed Arakawa-Schubert cumulus parameterization with convective downdrafts. NOAA Technical Report NWS/NCEP 99-01, U.S. Dept. of Commerce, Camp Springs, MD.

Neumann, C. J., B. R. Jarvinen, C. J. McAdie and J. D. Elms, 1999: Tropical cyclones of the North Atlantic ocean, 1871-1998. NCDC Historical Climatology Series, 6-2, 190 pp. (downloaded from <http://dss.ucar.edu/datasets/ds824.1/>)

New, M., M. Hulme, and P. Jones, 1999: Representing twentieth-century space-time climate variability. Part I: Development of a 1961-90 mean monthly terrestrial climatology. *J. Clim.*, **12**, 829-856.

Pierrehumbert, R. T., 1986. An essay on the parameterization of orographic gravity wave drag. Proceedings from ECMWF 1986 Seminar, Vol. I, 251-282.

Pincus, R. and S. A. Klein, 2000: Unresolved spatial variability and microphysical process rates in large-scale models. *J. Geophys. Res.*, **105**, 27059-27065.

Pincus, R., H. W. Barker, and J.-J. Morcrette, 2003: A fast, flexible, approximate technique for computing radiative transfer in inhomogeneous clouds. *J. Geophys. Res.*, **108**, 4376-4380, doi:10.1029/2002JD003322.

Ramachandran, S., V. Ramaswamy, G. L. Stenchikov, and A. Robock, 2000: Radiative impact of the Mount Pinatubo volcanic eruption: Lower stratospheric response. *J. Geophys. Res.*, **105**, 24409-24429.

Ramaswamy, V., and M. M. Bowen, 1994: Effect of changes in radiatively active species upon the

GFDL GAMDT

- lower stratospheric temperatures. *J. Geophys. Res.*, **99**, 18909-18921.
- Ramaswamy, V., and M. D. Schwarzkopf, 2002: Effects of ozone and well-mixed gases on annual-mean stratospheric temperature trends. *Geophys. Res. Lett.*, **29**, 2064, 10.1029/2002GL015141.
- Randel, D. L. and co-authors, 1996: A new global water vapor dataset. *Bull. Amer. Met. Soc.*, **77**, 1233-1246.
- Ropelewski, C. F. and M. S. Halpert, 1987: Global and regional scale precipitation patterns associated with the El Niño/Southern Oscillation. *Mon. Wea. Rev.*, **115**, 1606-1626.
- Rossow, W. B. and R. A. Schiffer, 1999: Advances in Understanding Clouds from ISCCP. *Bull. Amer. Met. Soc.*, **80**, 2261-2288.
- Rothman, L.S. and 30 co-authors, 2003: The HITRAN molecular spectroscopic database: edition of 2000 including updates through 2001. *J. Quant. Spectr. Rad. Transfer*, **82**, 5-44.
- Rotstayn, L. D., 1997: A physically based scheme for the treatment of stratiform clouds and precipitation in large-scale models. I: Description and evaluation of microphysical processes. *Quart. J. Roy. Meteor. Soc.*, **123**, 1227-1282.
- Rotstayn, L. D., 2000: On the “tuning” of autoconversion parameterizations in climate models. *J. Geophys. Res.*, **105**, 15495-15507.
- Rotstayn, L. D., B. F. Ryan, and J. Katzfey, 2000: A scheme for calculation of the liquid fraction in mixed-phase clouds in large-scale models. *Mon. Wea. Rev.*, **128**, 1070-1088.

Schwarzkopf, M. D. and V. Ramaswamy, 1999: Radiative effects of CH₄, N₂O, halocarbons and the foreign-broadened H₂O continuum: A GCM experiment. *J. Geophys. Res.*, **104**, 9467-9488.

Shapiro, R., 1970: Smoothing, filtering and boundary effects. *Rev. Geophys. Space Phys.*, **8**, 359-387.

Siebesma, A. P., C. S. Bretherton, A. Brown, A. Chlond, J. Cuxart, P. G. Duynkerke, H. Jiang, M. Khairoutdinov, D. Lewellen, C.-H. Moeng, E. Sanchez, B. Stevens, and D. E. Stevens, 2003: A large-eddy simulation intercomparison study of shallow cumulus convection. *J. Atmos. Sci.*, **60**, 1201-1219.

Siebesma, A. P., C. Jakob, G. Lenderink, R. Neggers, J. Teixeira, J. Calvo, A. Chlond, H. Grenier, C. Jones, M. Koehler, H. Kitagawa, P. Marquet, A. Lock, F. Mueller, D. Olmeda, C. Severijn, 2004: Cloud representation in general circulation models over the Northern Pacific Ocean: A EUROCS intercomparison study. submitted to *Quart. J. Roy. Meteor. Soc.*

Simmons, A. J. and D. M. Burridge, 1981: An energy and angular-momentum conserving vertical finite-difference scheme and hybrid vertical coordinates. *Mon. Wea. Rev.*, **109**, 758-766.

Slingo, A., 1989: A GCM parameterization for the shortwave radiative properties of water clouds. *J. Atmos. Sci.*, **46**, 1419-1427.

Soden, B. J. and F. P. Bretherton, 1993: Upper troposphere relative humidity from the GOES 6.7 μm channel: Method and climatology for July 1987. *J. Geophys. Res.*, **98**, 16,669-16,688.

Stackhouse, P. W., Jr., S. J. Cox, S. K. Gupta, J. C. Mikovitz, and M. Chiacchio, 2003: The WCRP/GEWEX Surface Radiation Budget Data Set Release 2: A 1 degree resolution, 12 year flux climatology. in preparation.

Stern, W. F. and R. T. Pierrehumbert, 1988: The impact of an orographic gravity wave drag parameterization on extended range predictions with a GCM. Preprints to the 8th annual conference on Numerical Weather Prediction, Baltimore, American Meteorological Society, 745-750.

Stern, W. F. and K. Miyakoda, 1995: Feasibility of seasonal forecasts inferred from multiple GCM Simulations. *J. Clim.*, **8**, 1071-1085.

Sud, Y. C. and G. K. Walker, 1999: Microphysics of clouds with the relaxed Arakawa-Schubert scheme (McRAS). Part I: Design and evaluation with GATE Phase III Data. *J. Atmos. Sci.*, **56**, 3196-3220.

Taylor, J. P., J. M. Edwards, M. D. Glew, P. Hignett, and A. Slingo, 1996: Studies with a flexible new radiation code. Part II: Comparisons with aircraft short-wave observations. *Quart. J. Roy. Meteor. Soc.*, **122**, 839-861.

Taylor, K. E., 2001: Summarizing multiple aspects of model performance in a single diagram. *J. Geophys. Res.*, **106**, 7183-7192.

Thompson, D. W. and J. M. Wallace, 1998: The arctic oscillation signature in the winter time geopotential height and temperature fields. *Geophys. Res. Lett.*, **25**, 1297-1300.

Thompson, D. and J. M. Wallace, 2000 Annular modes in the extratropical circulation. Part I:

GFDL GAMDT

Month-to-month variability. *J. Clim.*, **13**, 1000-1016.

Tiedtke, M., 1993: Representation of clouds in large-scale models. *Mon. Wea. Rev.*, **121**, 3040-3061.

Tokioka, T., K. Yamazaki, A. Kitoh, and T. Ose, 1988: The equatorial 30-60 day oscillation and the Arakawa-Schubert penetrative cumulus parameterization. *J Meteor. Soc. Japan*, **66**, 883-901.

Tompkins, A. M., 2002: A prognostic parameterization for the subgrid-scale variability of water vapor and clouds in large-scale models and its use to diagnose cloud cover. *J. Atmos. Sci.*, **59**, 1917-1942.

Trenberth, K. E., 1997: The definition of El Niño. *Bull. Amer. Met. Soc.*, **78**, 2771-2777.

Trenberth, K. E., and J. M. Caron, 2001: Estimates of meridional atmosphere and ocean heat transports. *J. Clim.*, **14**, 3433-3443.

Vitart, F., J. L. Anderson, and W. F. Stern, 1997: Simulation of interannual variability of tropical storm frequency in an ensemble of GCM integrations. *J. Clim.*, **10**, 745-760.

Vitart, F., and T. N. Stockdale, 2001: Seasonal forecasting of tropical storms using coupled GCM integrations. *Mon. Wea. Rev.*, **129**, 2521-2537.

Waliser, D., W. Lau, W. Stern, and C. Jones, 2003: Potential predictability of the Madden-Julian oscillation. *Bull. Amer. Met. Soc.*, **84**, 33-50.

Walsh, J. E., V. M. Kattsov, W. L. Chapman, V. Govorkova, and T. Pavlova, 2002: Comparison of

GFDL GAMDT

Arctic climate simulations by uncoupled and coupled global models. *J. Clim.*, **15**, 1429-1446.

Warren, S. G., C. J. Hahn, J. London, R. M. Chevin, and R. L. Jenne, 1986: Global distribution of total cloud cover and cloud type amounts over land. NCAR Technical Note TN-273+STR, Boulder, CO, 29 pp. + 200 maps. [Available from Carbon Dioxide Information Analysis Center, Oak Ridge, Tennessee.]

Warren, S. G., C. J. Hahn, J. London, R. M. Chevin, and R. L. Jenne, 1988: Global distribution of total cloud cover and cloud type amounts over ocean. NCAR Technical Note TN-317+STR, Boulder, CO, 44 pp. + 170 maps. [Available from Carbon Dioxide Information Analysis Center, Oak Ridge, Tennessee.]

Webb, M., C. Senior, S. Bony, and J.-J. Morcrette, 2001: Combining ERBE and ISCCP data to assess clouds in the Hadley Centre, ECMWF, and LMD atmospheric climate models. *Clim. Dyn.*, **17**, 905-922.

Weng, F., N. C. Grody, R. Ferraro, A. Basist, and D. Forsyth, 1997: Cloud liquid water climatology from the Special Sensor Microwave/Imager. *J. Clim.*, **10**, 1086-1098.

Wood, N. and P. Mason, 1993: The pressure force induced by neutral turbulent flow over hills. *Quart. J. Roy. Meteor. Soc.*, **119**, 1233-1267.

Woodruff, S. D., R. J. Slutz, R. L. Jenne and P. M. Steurer, 1987: A Comprehensive Ocean-Atmosphere Data Set. *Bull. Amer. Met. Soc.*, **68**, 1239-1239.

Wyman, B. L., 1996: A step-mountain coordinate general circulation model: Description and val-

idation of medium-range forecasts. *Mon. Wea. Rev.*, **124**, 102-121.

Xie, P. and P. A. Arkin, 1997: Global precipitation: A 17-year monthly analysis based on gauge observations, satellite estimates, and numerical model outputs. *Bull. Amer. Met. Soc.*, **78**, 2539-2558.

Zhang, Y.-C., W. B. Rossow, A. A. Lacis, V. Oinas, and M. I. Mishchenko, 2003: Calculation of radiative flux profiles from the surface to top-of-atmosphere based on ISCCP and other global datasets: Refinements of the radiative transfer model and the input data. in preparation for *J. Geophys. Res.*

Table captions

Table 1. Brief description of AM2/LM2 components.

Table 2. Coefficients a_k and b_k for calculation of interface level values. The coefficients are used in the Simmons-Burridge (1981) formula $p = a_k + b_k * p_s$, where p is pressure and p_s is surface pressure. The pressures p and geopotential heights z of interface levels using a scale height of 7.5 km and $p_s = 1013.25$ hPa are also shown.

Table 3. Selected global annual mean radiation budget and hydrologic quantities. Observational data sources are ERBE: Harrison et al. (1990); GEWEX: Stackhouse et al. (2004); GISS: Zhang et al. (2003); KT: Kiehl and Trenberth (1997); NVAP: Randel et al. (1996), GR: Greenwald et al. (1993); WG: Weng et al. (1997); ISCCP: Rossow and Schiffer (1999); SFC: Warren et al. (1986,1988); CMAP: Xie and Arkin (1997); GPCP: Huffman et al. (1997).

Component	Description
Dynamics	B-grid model, 2.5° longitude by 2.0° latitude 24 vertical levels with the effective model top at about 40 km
Radiation	Diurnal cycle with full radiation calculation every 3 hours Effects of H ₂ O, CO ₂ , O ₃ , O ₂ , N ₂ O, CH ₄ , and 4 halocarbons included
<i>Longwave:</i>	Simplified Exchange Approximation (Schwarzkopf and Ramaswamy 1999) Clough et al. (1992) CKD 2.1 H ₂ O continuum parameterization
<i>Shortwave:</i>	Exponential Sum Fit with 18 bands (Freidenreich and Ramaswamy 1999) Liquid cloud radiative properties from Slingo (1989) Ice cloud radiative properties from Fu and Liou (1993)
<i>Aerosols:</i>	Prescribed monthly three-dimensional climatology from chemical transport models Species represented include sulfate, hydrophilic and hydrophobic car- bon, dust, and sea salt
Clouds	3 prognostic tracers: cloud liquid, cloud ice, and cloud fraction Cloud microphysics from Rotstayn (1997) Cloud macrophysics from Tiedtke (1993)

Table 1. Brief description of AM2/LM2 components.

Component	Description
Convection	<p>Relaxed Arakawa Schubert (Moorthi and Suarez 1992)</p> <p>Detrainment of cloud liquid, ice and fraction from convective updrafts into stratiform clouds</p> <p>A lower bound imposed on lateral entrainment rates for deep convective updrafts (Tokioka et al. 1988)</p> <p>Convective momentum transport represented by vertical diffusion proportional to the cumulus mass flux</p>
Vertical diffusion	<p>Surface and stratocumulus convective layers represented by a K-profile scheme with prescribed entrainment rates (Lock et al. 2000)</p> <p>Surface fluxes from Monin-Obukhov similarity theory</p> <p>Gustiness enhancement to wind speed used in surface flux calculations (Beljaars 1995)</p> <p>Enhanced near-surface mixing in stable conditions</p> <p>Orographic roughness effects included</p>
Gravity Wave Drag	Orographic drag from Stern and Pierrehumbert (1988)
Land Model	<p>Isothermal surface (soil-snow-vegetation)</p> <p>3 water stores: snow, root zone and ground water</p> <p>18 soil-temperature levels to 6 m total depth</p> <p>Stomatal control of evapotranspiration</p> <p>Latent heat storage in soil</p> <p>Surface parameters dependent on 8 soil and 8 vegetation types</p>

Table 1 (cont.). Brief description of AM2/LM2 components.

<i>k</i>	<i>a_k</i> (Pa)	<i>b_k</i>	<i>p</i> (hPa)	<i>z</i> (km)
1	0	0	0	-
2	903.45	0	9	35.40
3	3474.8	0	35	25.30
4	7505.6	0	75	19.52
5	12787	0	128	15.52
6	19111	0	191	12.51
7	21855	0.043568	263	10.12
8	22884	0.11023	341	8.18
9	22776	0.19223	423	6.56
10	21716	0.28177	503	5.26
11	20073	0.36950	575	4.25
12	18110	0.45324	640	3.44
13	16005	0.53163	699	2.79
14	13878	0.60387	751	2.25
15	11813	0.66956	797	1.80
16	9865.9	0.72852	837	1.43
17	8074.0	0.78080	872	1.13
18	6458.1	0.82660	902	0.87
19	5028.0	0.86621	928	0.66
20	3784.6	0.90004	950	0.48
21	2722.0	0.92854	968	0.34
22	1829.0	0.95221	983	0.23
23	1090.2	0.97163	995	0.13
24	487.56	0.98735	1005	0.06
25	0	1	1013	0

Table 2. Coefficients *a_k* and *b_k* for calculation of interface level values. The coefficients are used in the Simmons-Burridge (1981) formula $p = a_k + b_k * p_s$, where *p* is pressure and *p_s* is surface pressure. The pressures *p* and geopotential heights *z* of interface levels using a scale height of 7.5 km and *p_s* = 1013.25 hPa are also shown.

GFDL GAMDT

Measure	Source	Observation	AM2/LM2
<u>Top of Atmosphere Radiation Budget ($W\ m^{-2}$)</u>			
Shortwave absorbed	ERBE	240.2	235.7
Outgoing longwave radiation	ERBE	235.3	235.3
Clear-sky shortwave absorbed	ERBE	288.4	289.1
Clear-sky outgoing longwave radiation	ERBE	264.8	260.0
Shortwave cloud forcing	ERBE	-48.2	-53.4
Longwave cloud forcing	ERBE	29.5	24.7
<u>Surface Energy Budget ($W\ m^{-2}$)</u>			
Shortwave absorbed	GEWEX/GISS	164.6/165.2	159.8
Net longwave	GEWEX/GISS	-47.1/-50.9	-57.8
Clear-sky shortwave absorbed	GEWEX/GISS	214.7/218.4	216.9
Clear-sky downward longwave	GEWEX/GISS	309.6/313.5	313.9
Shortwave cloud forcing	GEWEX/GISS	-50.1/-53.3	-57.2
Longwave down cloud forcing	GEWEX/GISS	35.6/31.1	24.5
Sensible heat flux	KT	24	18.7
Latent heat flux	KT	78	82.2
<u>Hydrologic Quantities</u>			
Column integrated water vapor ($kg\ m^{-2}$)	NVAP	24.5	23.4
Column integrated oceanic cloud liquid ($g\ m^{-2}$)	GR/WG	76.2/63.4	77.1
Column integrated cloud ice ($g\ m^{-2}$)	-	-	37.6
Total cloud amount (fraction)	ISCCP/SFC	0.69/0.62	0.66
Surface Precipitation ($mm\ d^{-1}$)	CMAP/GPCP	2.68/2.65	2.84

Table 3. Selected global annual mean radiation budget and hydrologic quantities. Observational data sources are ERBE: Harrison et al. (1990); GEWEX: Stackhouse et al. (2004); GISS: Zhang et al. (2003); KT: Kiehl and Trenberth (1997); NVAP: Randel et al. (1996), GR: Greenwald et al. (1993); WG: Weng et al. (1997); ISCCP: Rossow and Schiffer (1999); SFC: Warren et al. (1986,1988); CMAP: Xie and Arkin (1997); GPCP: Huffman et al. (1997).

Figure captions

Figure 1. Long-term annual and zonal mean temperature difference between NCEP/NCAR reanalysis climatology and AM2/LM2 (AM2/LM2 minus NCEP). Contour interval is 0.5 K.

Figure 2. Long-term annual mean 2 m temperature difference between CRU climatology and AM2/LM2 (AM2/LM2 minus CRU). Contour interval is 2 K.

Figure 3. Long-term mean 2 m temperature difference for North America between CRU climatology and AM2/LM2 (AM2/LM2 minus CRU) for a) December-January-February (DJF) and b) June-July-August (JJA). Contour interval is 2 K.

Figure 4. Long-term annual and zonal mean zonal wind in m s^{-1} for (a) NCEP/NCAR reanalysis, (b) AM2/LM2, and (c) AM2/LM2 minus NCEP. Contour interval is 5 m s^{-1} in (a) and (b) and 1 m s^{-1} in (c).

Figure 5. Long-term annual and zonal mean zonal wind stress in Pa over the ocean for the ship-based climatology of COADS (blue) (daSilva et al. 1994; Woodruff et al. 1987), ECMWF reanalysis (red) (Gibson et al. 1997), the ERS satellite scatterometer (green) (CERSAT-IFREMER 2002), and AM2/LM2 (black). The sign convention is such that a positive stress indicates an easterly stress on the atmosphere and a westerly stress on the ocean.

Figure 6. Long-term Northern Hemisphere DJF mean SLP minus 1013.25 hPa for (a) AM2/LM2, (b) NCEP/NCAR reanalysis, and (c) AM2/LM2 minus NCEP. Contour interval is 3 hPa for (a) and (b) and 1 hPa for (c); the zero contour is not plotted in (c). Note that regions with mean surface pressure below 950 hPa have been masked.

Figure 7. Long-term DJF mean departure of 500 hPa geopotential height from its zonal mean for (a) AM2/LM2, (b) NCEP/NCAR reanalysis climatology, and (c) AM2/LM2 minus NCEP. Contour interval is 25 m in (a) and (b) and 10 m in (c). Statistics at the bottom of (a) and (b) include the Northern Hemisphere mean and standard deviation. Statistics at the bottom of (c) include the difference in Northern Hemisphere means, the root mean square error, and the correlation coefficient.

Figure 8. Annual long-term mean precipitation in mm d⁻¹ for (a) AM2/LM2, (b) CMAP observations, and (c) AM2/LM2 minus CMAP. Statistics at the bottom of (a) and (b) include the global mean and standard deviation. Statistics at the bottom of (c) include the difference in global means, the correlation coefficient, and the root mean square error.

Figure 9. Annual long-term mean outgoing longwave radiation (OLR) in W m⁻² for (a) AM2/LM2, (b) ERBE observations, and (c) AM2/LM2 minus ERBE. Statistics at the bottom of (a) and (b) include the global mean and standard deviation. Statistics at the bottom of (c) include the difference in global means, the correlation coefficient, and the root mean square error.

Figure 10. Annual long-term mean absorbed solar radiation (SWAbs) in W m⁻² for (a) AM2/LM2, (b) ERBE observations, and (c) AM2/LM2 minus ERBE. Statistics at the bottom of (a) and (b) include the global mean and standard deviation. Statistics at the bottom of (c) include the difference in global means, the correlation coefficient, and the root mean square error.

Figure 11. Annual long-term mean total cloud amount (fraction) for (a) AM2/LM2, (b) ISCCP observations, and (c) AM2/LM2 minus ISCCP. Statistics at the bottom of (a) and (b) include the global mean and standard deviation. Statistics at the bottom of (c) include the difference in global

means, the correlation coefficient, and the root mean square error. Note that these statistics have been computed only over the domain 60°S-60°N, as high latitude ISCCP data is unreliable.

Figure 12. Annual long-term mean upper tropospheric humidity in percent for (a) AM2/LM2, (b) TOVS observations, and (c) TOVS minus AM2/LM2. Statistics at the bottom of (a) and (b) indicate the global mean. Statistics at the bottom of (c) include the difference in global means, the correlation coefficient, and the root mean square error.

Figure 13. Distributions of the regression coefficients of precipitation rate versus the standardized NINO3 SST index, as computed using the ensemble mean of the 10-member AMIP-style integrations with the AM2/LM2 for 1951-2000 (upper panel) and the GPCP dataset for 1979-2000, both for the December-January-February season. Contour interval: 1 mm d⁻¹. Zero contour is omitted. Contours for -0.5 and +0.5 mm d⁻¹ are inserted.

Figure 14. Distributions of the regression coefficients of 200 hPa height versus the standardized NINO3 SST index, as computed using the ensemble mean of the 10-member AMIP-style integrations with the AM2/LM2 (upper panels) and NCEP reanalyses (lower panels) for the December-January-February season of the 1951-2000 period. Results for the northern and southern extratropics are shown in the left and right panels, respectively. Contour interval is 5 m. The zero-contour is not plotted.

Figure 15. Taylor diagram depicting the relationships between the observed DJF 200 hPa height anomalies in the North Pacific / North American sector (20°-70°N, 60°-180°W) during selected ENSO events and the corresponding ensemble-mean patterns as simulated in the 10-member AMIP-style runs with the AM2/LM2. Results for individual warm and cold ENSO events are pre-

sented using red and blue dots, respectively. The two-digit label for each dot indicates the year of the event in question. The spatial correlation coefficient is given by the cosine of the angle between the abscissa and the straight line joining the origin and the dot representing the event of interest; correlation values are given along the outer solid arc. The ratio between the simulated and observed spatial variances is given by the distance between the dot and origin; inner and outer solid arcs indicate ratios of 1 and 1.5, respectively. The root mean square (rms) difference between the simulated and observed pattern, as normalized by the spatial variance of the observed field, is given by the distance between the dot and the point with coordinates (1,0) in the diagram; inner and outer dotted arcs indicate normalized rms differences of 0.5 and 1, respectively.

Figure 16. Scatterplots of the precipitation anomalies in three monsoon regions [IND - Indian; AUS - northern Australia; SEA - southeast Asia; boundaries of these regions are depicted in Figure 3 of Lau and Nath (2000)] versus the NINO3 SST anomalies. The abscissa in all panels represents the standardized SST anomaly in the NINO3 region. The ordinate axis represents the standardized precipitation anomaly in IND during the JJA (left panels), and in SEA (middle panels) and AUS (right panels) during the DJF season. The upper panels are based on AM2/LM2 output for the 1951-2000 period. The lower panels show the observational estimates provided by GPCP for the shorter period of 1979-2000. In each panel, the anomalies of precipitation and NINO3 index for a given year are jointly depicted by a small dot or square. The outstanding warm and cold ENSO events are highlighted using colored dots and squares, respectively. The data for all remaining years are plotted using black dots. The correlation coefficient for the data entries in each panel is shown in the upper right corner of that panel. Correlation values based on all available years are given in parentheses. Correlation values based on the available warm and cold ENSO events only are given without parentheses.

Figure 17. Spatial pattern of anomalies in sea level pressure (SLP, contours) and surface temperature (color shading) associated with a 1 hPa increase in an index of the Northern Annular Mode (NAM), also referred to as the Arctic Oscillation. The anomalies shown are from the months of November through April only. The SLP anomalies are computed by multiplying the linear regression coefficients at each grid point by a 1 hPa increase in a NAM index. The shading indicates the surface air temperature anomalies in °C associated with a 1 hPa increase of a NAM index and is computed in a similar manner. The NAM is defined by computing an empirical orthogonal function (EOF) of SLP for all points north of 20°N. A NAM index is then calculated as the difference between the minimum and maximum of the spatial pattern of the first EOF multiplied by its associated time series, thereby yielding an index with units hPa. (a) Spatial pattern NAM anomalies for AM2/LM2. A 10 member ensemble of experiments was conducted using observed SST variations from 1951 to 2000. For each ensemble member a NAM pattern was computed as described above. The spatial pattern shown is the 10 member ensemble mean of the NAM regression patterns. The temperature shown is the 2 m surface air temperature over both land and ocean. (b) Similar to (a) but for observational data. The EOF of SLP is adapted from Thompson and Wallace, (1998); the surface temperature data is from Jones (1994). Surface air temperature is used over land, while SST is used over oceanic regions including ice-covered areas.

Figure 18. Frequency of tropical cyclone genesis for (a) AM2/LM2 and (b) observations. Units are number of storms per year in a box of size 4° latitude by 5° longitude.

Figure 19. Wave frequency spectra of 5°N to 5°S 200 hPa zonal wind variance for AM2/LM2 (top) and NCEP reanalyses (bottom). Contour interval is 40 m²s⁻².

Figure 20. Composite Northern Hemisphere winter (November-April) Madden-Julian Oscillation

from 30-90 day filtered precipitation in mm d⁻¹. Maps based on AM2/LM2 are shown in the left column and those based on CMAP observations in right column. Sequential maps are 10 day means centered on lags of -30 days, -15 days, 0 days, +15 days, and +30 days. The superimposed green dashed lines indicate propagation of the disturbance. Note that the values for AM2/LM2 values have been enhanced by a factor of 2.

Figure 21. Taylor diagrams for selected variables comparing the skill of AM2/LM2 (red circle) in reproducing the observed climatology to that of older GFDL models (MCM and DERF, green and orange circles respectively) and other models participating in AMIP II (CCM3.5, ECHAM4, ECMWF, and HADAM3). Note that all non-GFDL models are plotted with a blue diamond to prevent unique identification. The selected variables include those associated with surface climate (SLP, land surface air temperature, and oceanic wind stress, top row), water cycle and clouds (precipitation, shortwave cloud forcing, and total cloud amount, middle row), and upper tropospheric circulation (200 hPa eddy geopotential and zonal wind, bottom row). The observational sources for these data include the NCEP reanalyses for SLP and 200 hPa eddy geopotential and zonal wind, ECMWF reanalyses for oceanic wind stress, ERBE for cloud radiative forcing, ISCCP for total cloud amount, CMAP for precipitation and CRU for land surface air temperature. Beneath each variable name is an indication of the geographical domain and season used in the calculation.

Figure 22. Poleward oceanic heat transport in petawatts (10¹⁵ W) from observational based estimates and implied by AM2/LM2 (dark black line). The observed estimates are derived from atmospheric data (Trenberth and Caron 2001; red lines with dashed lines indicating plus or minus one standard error; based on NCEP-derived products) or oceanic data (Ganachaud and Wunsch 2003). Results are shown for the a) Atlantic, b) Indo-Pacific, and c) world ocean basins.

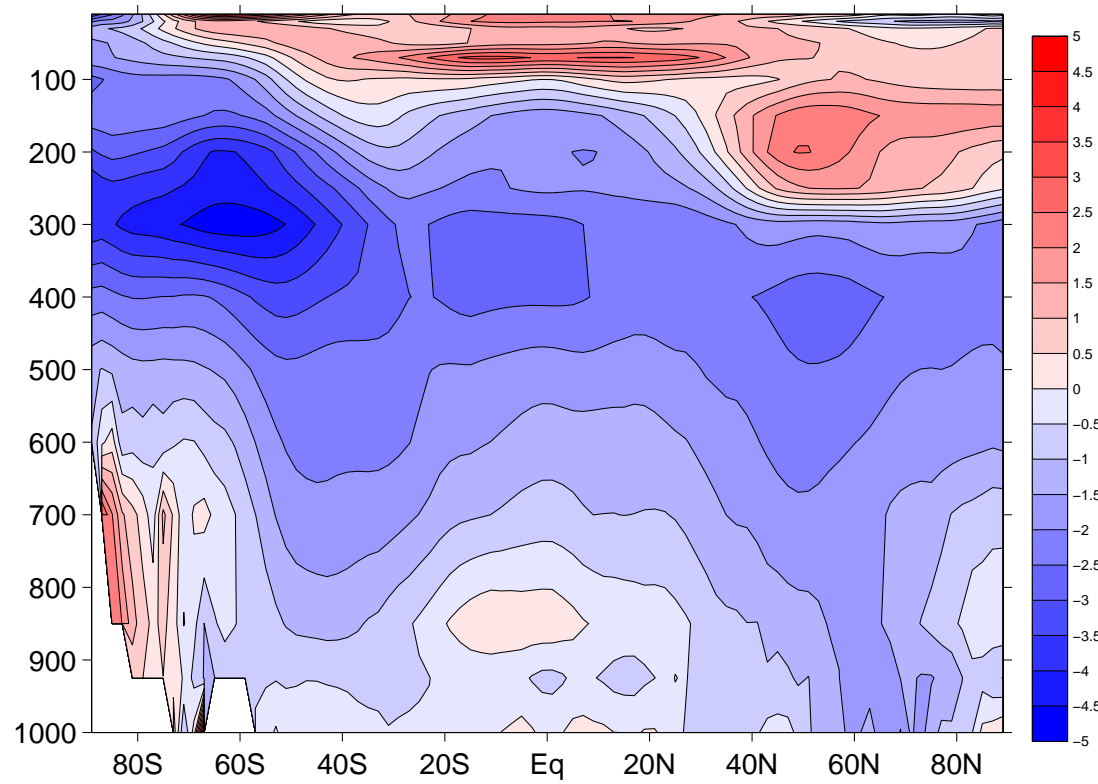


Figure 1. Long-term annual and zonal mean temperature difference between NCEP/NCAR reanalysis climatology and AM2/LM2 (AM2/LM2 minus NCEP). Contour interval is 0.5 K.

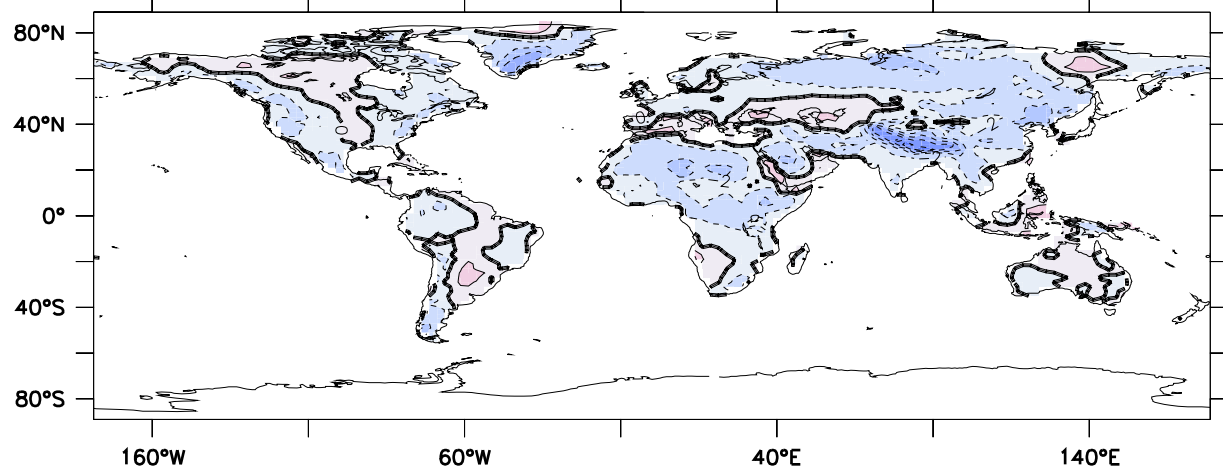


Figure 2. Long-term annual mean 2 m temperature difference between CRU climatology and AM2/LM2 (AM2/LM2 minus CRU). Contour interval is 2 K.

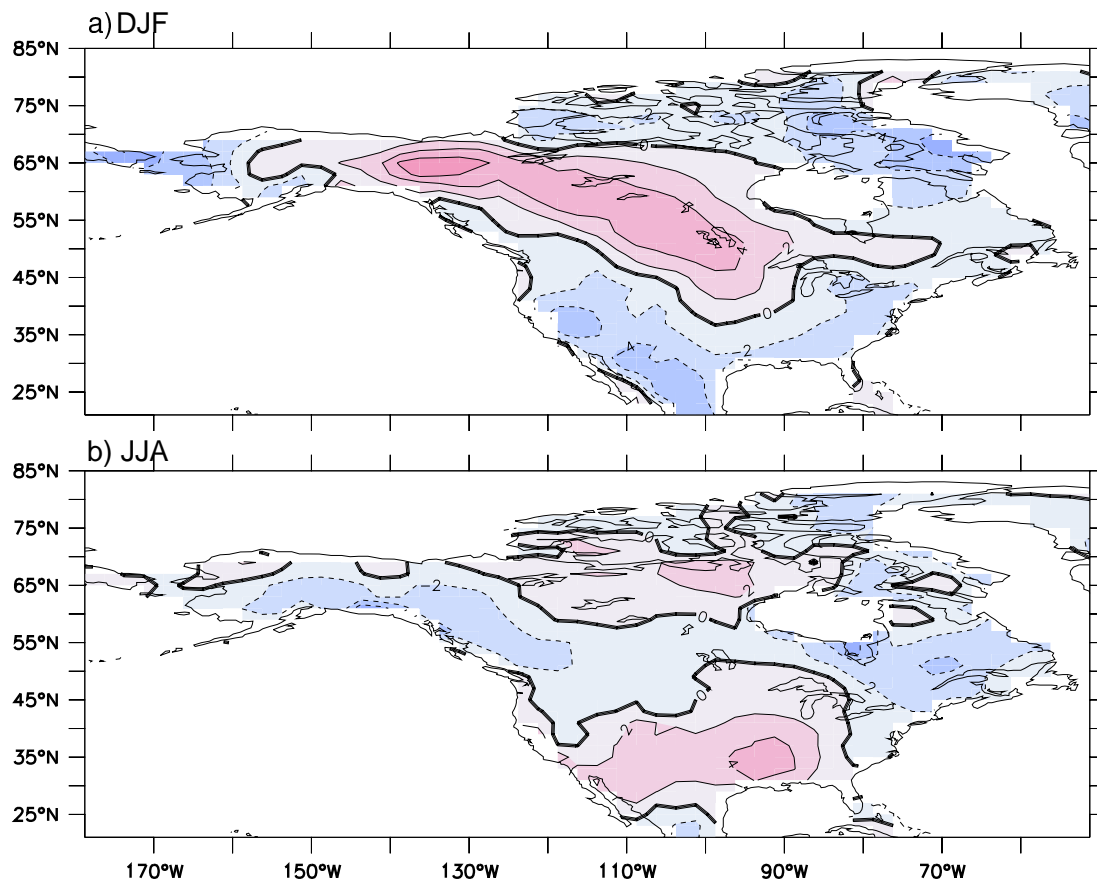


Figure 3. Long-term mean 2 m temperature difference for North America between CRU climatology and AM2/LM2 (AM2/LM2 minus CRU) for a) December-January-February (DJF) and b) June-July-August (JJA). Contour interval is 2 K.

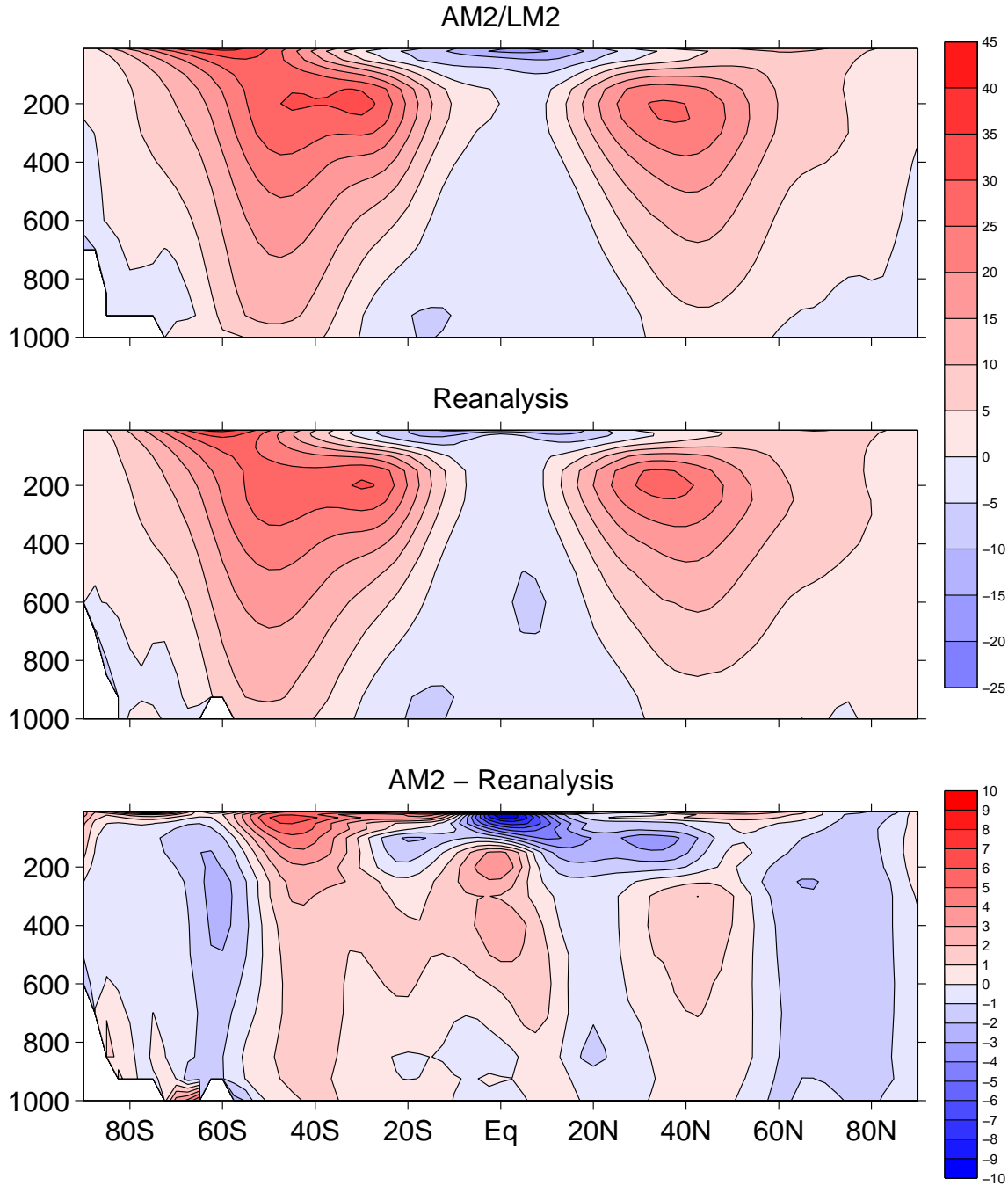


Figure 4. Long-term annual and zonal mean zonal wind in m s^{-1} for (a) NCEP/NCAR reanalysis, (b) AM2/LM2, and (c) AM2/LM2 minus NCEP. Contour interval is 5 m s^{-1} in (a) and (b) and 1 m s^{-1} in (c).

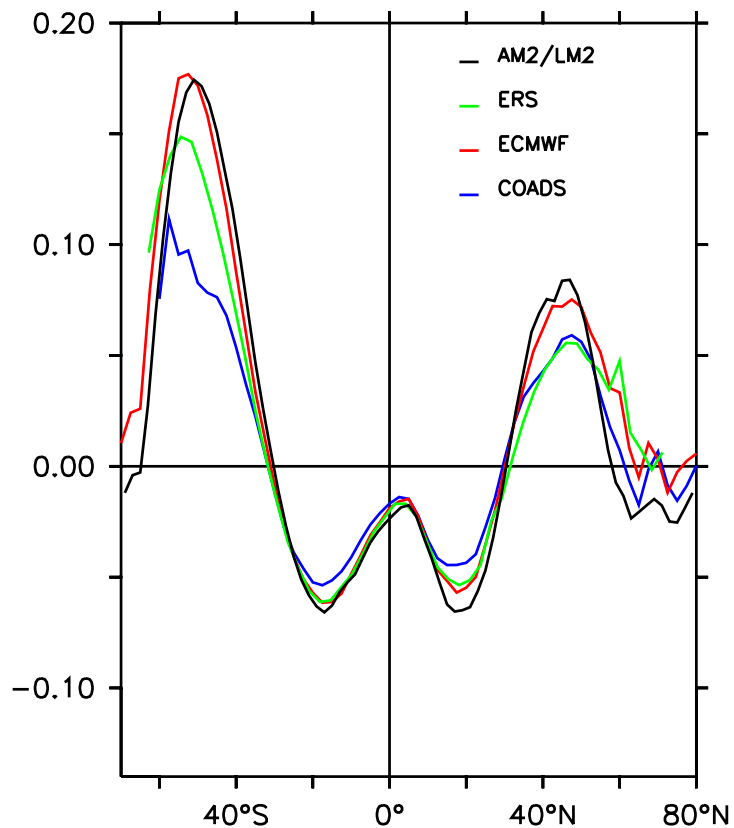


Figure 5. Long-term annual and zonal mean zonal wind stress in Pa over the ocean for the ship-based climatology of COADS (blue) (daSilva et al. 1994; Woodruff et al. 1987), ECMWF reanalysis (red) (Gibson et al. 1997), the ERS satellite scatterometer (green) (CERSAT-IFREMER 2002), and AM2/LM2 (black). The sign convention is such that a positive stress indicates an easterly stress on the atmosphere and a westerly stress on the ocean.

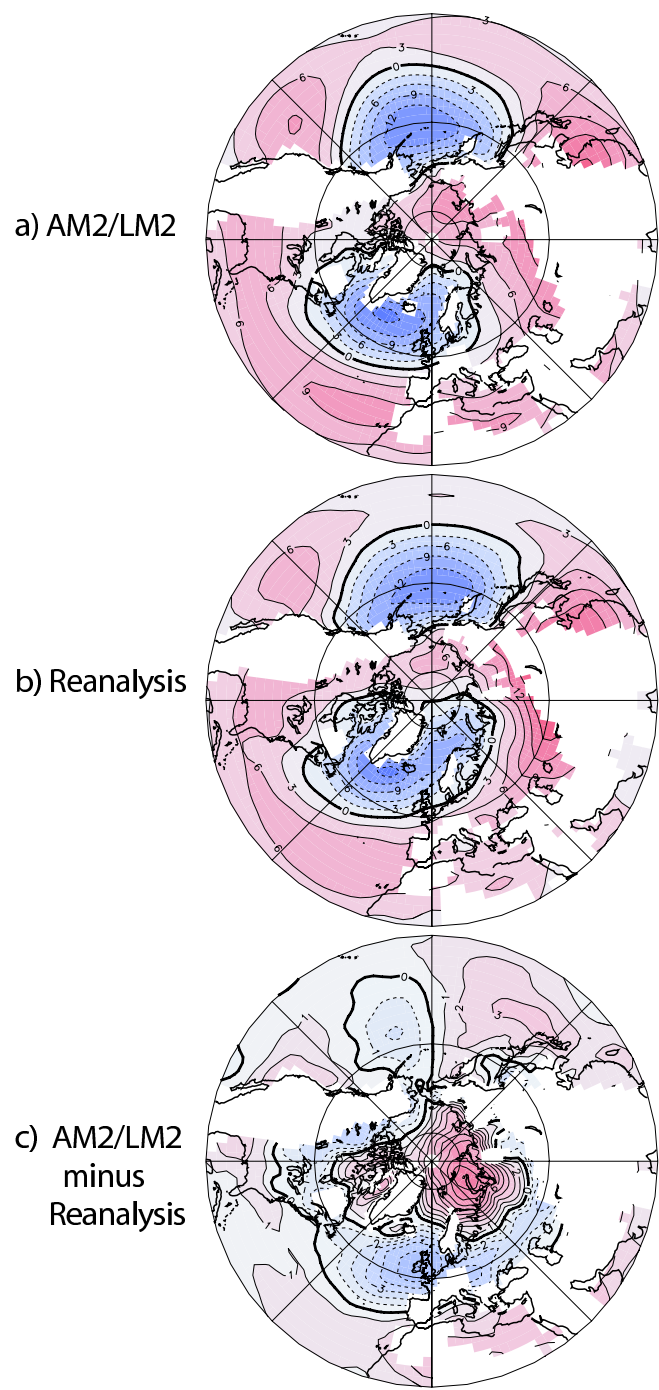


Figure 6. Long-term Northern Hemisphere DJF mean SLP minus 1013.25 hPa for (a) AM2/LM2, (b) NCEP/NCAR reanalysis, and (c) AM2/LM2 minus NCEP. Contour interval is 3 hPa for (a) and (b) and 1 hPa for (c); the zero contour is not plotted in (c). Note that regions with mean surface pressure below 950 hPa have been masked.

GFDL GAMDT

Z^*500 , djf

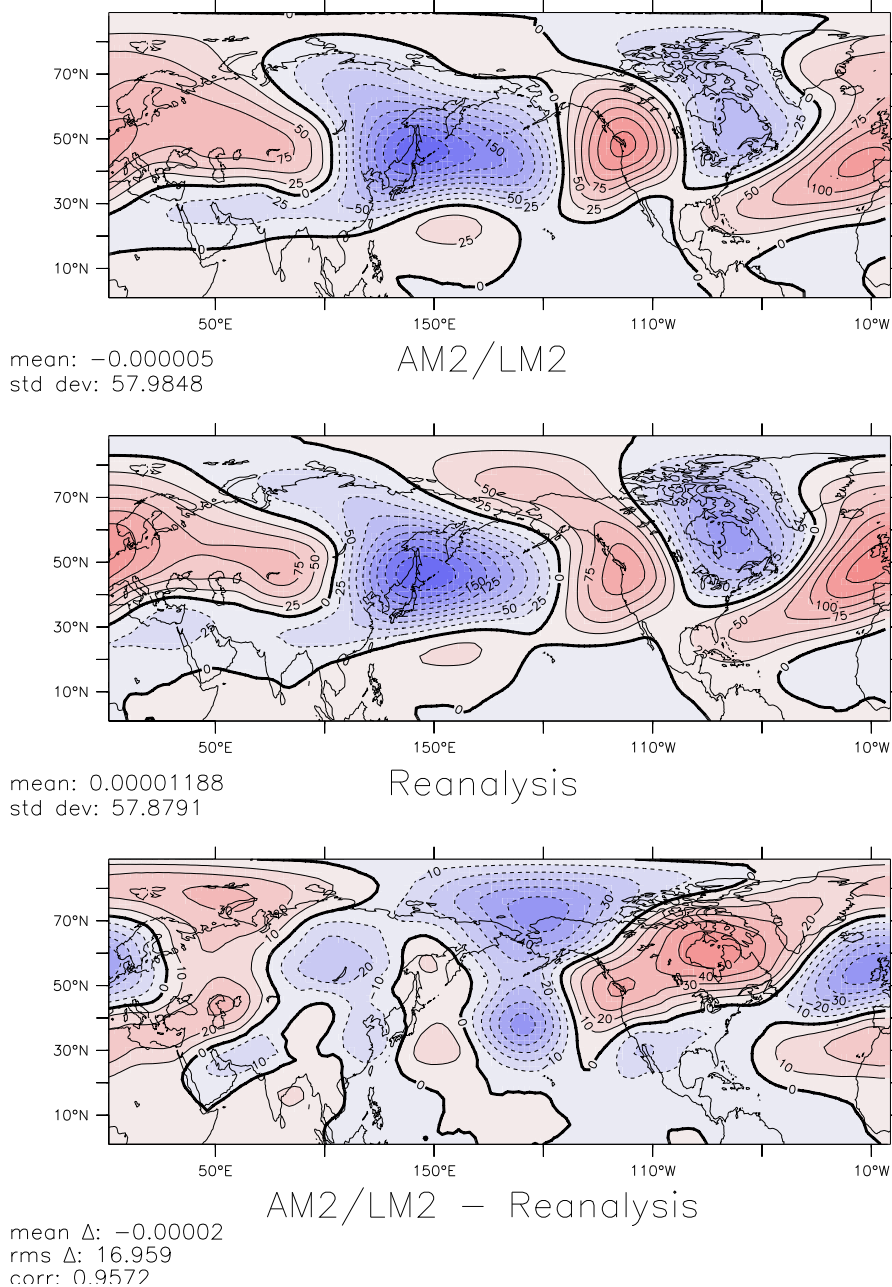
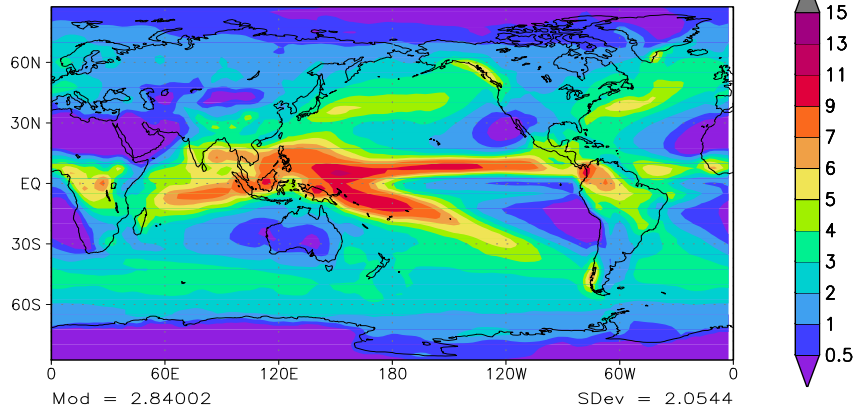


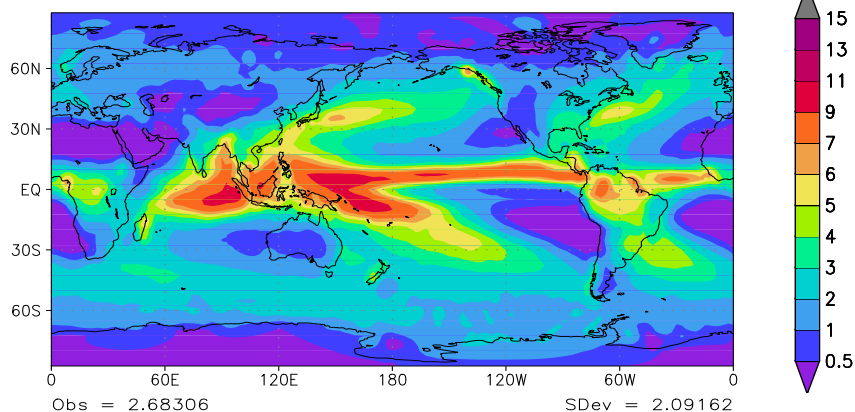
Figure 7. Long-term DJF mean departure of 500 hPa geopotential height from its zonal mean for (a) AM2/LM2, (b) NCEP/NCAR reanalysis climatology, and (c) AM2/LM2 minus NCEP. Contour interval is 25 m in (a) and (b) and 10 m in (c). Statistics at the bottom of (a) and (b) include the Northern Hemisphere mean and standard deviation. Statistics at the bottom of (c) include the difference in Northern Hemisphere means, the root mean square error, and the correlation coefficient.

ANN PRECIP (mm/d)

AM2/LM2



CMAP



AM2/LM2 minus CMAP

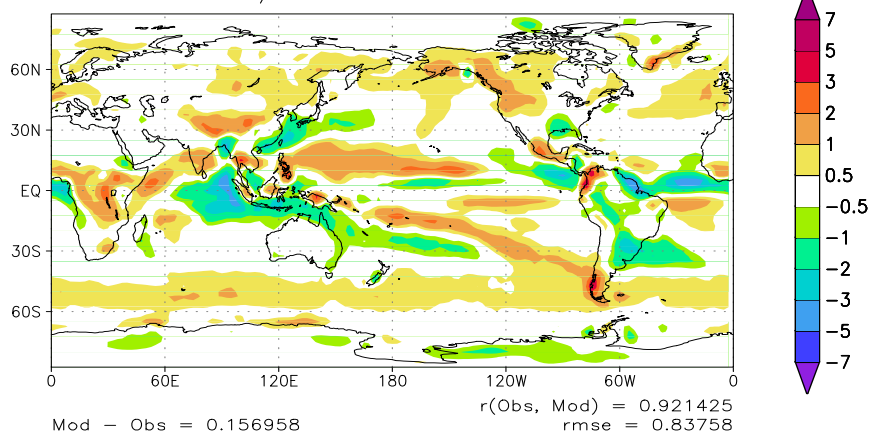


Figure 8. Annual long-term mean precipitation in mm d^{-1} for (a) AM2/LM2, (b) CMAP observations, and (c) AM2/LM2 minus CMAP. Statistics at the bottom of (a) and (b) include the global mean and standard deviation. Statistics at the bottom of (c) include the difference in global means, the correlation coefficient, and the root mean square error.

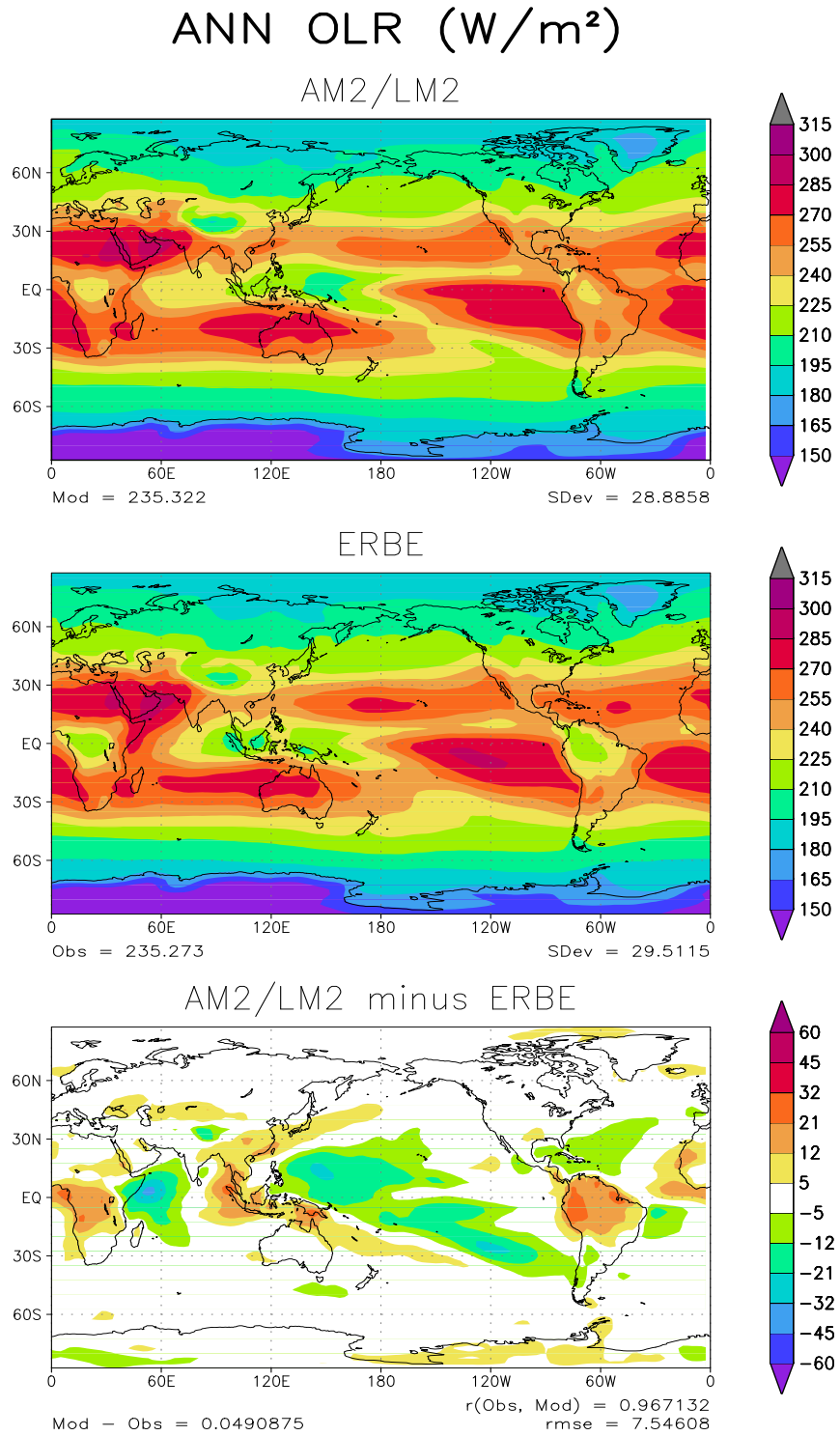


Figure 9. Annual long-term mean outgoing longwave radiation (OLR) in W m^{-2} for (a) AM2/LM2, (b) ERBE observations, and (c) AM2/LM2 minus ERBE. Statistics at the bottom of (a) and (b) include the global mean and standard deviation. Statistics at the bottom of (c) include the difference in global means, the correlation coefficient, and the root mean square error.

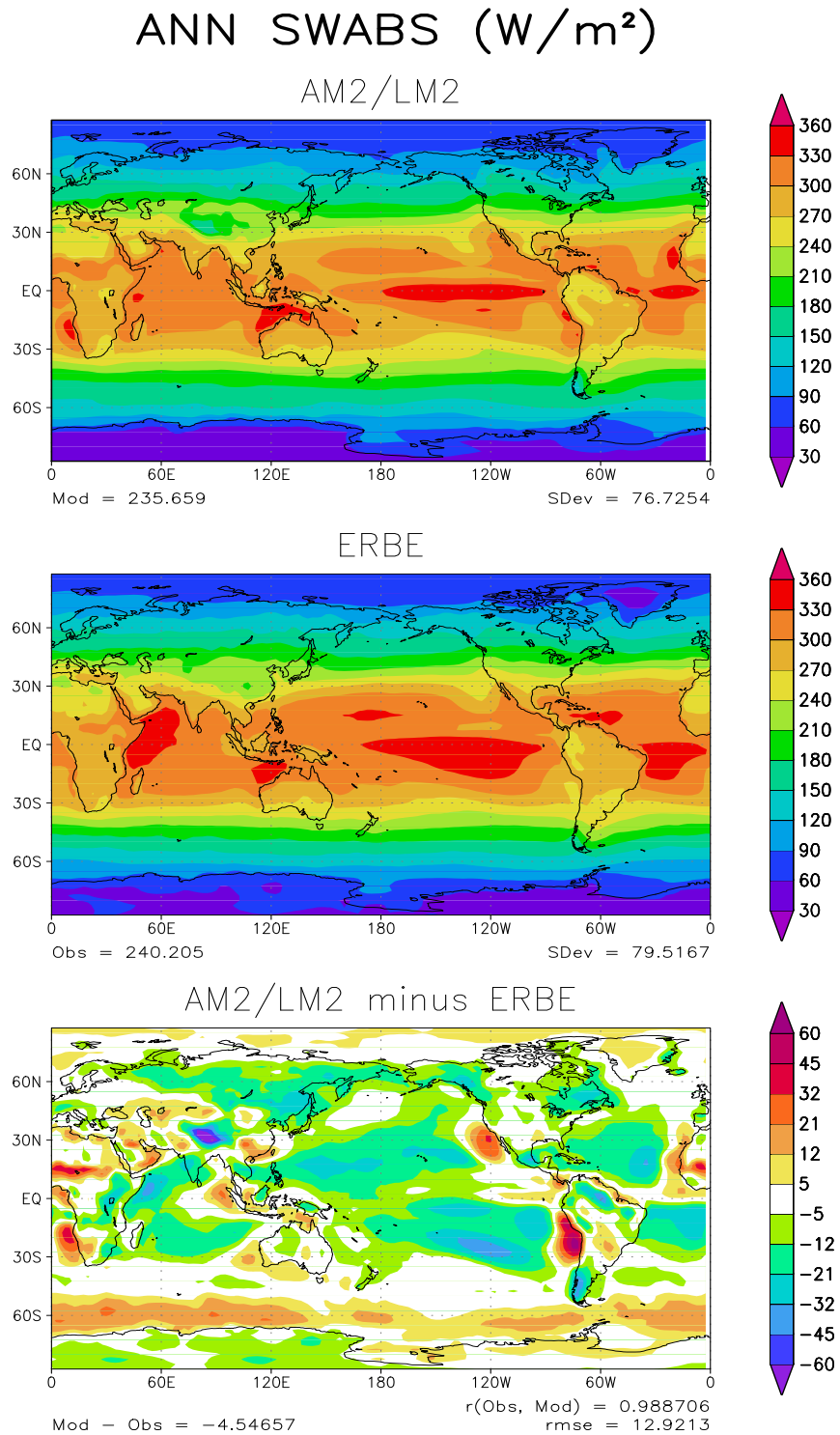
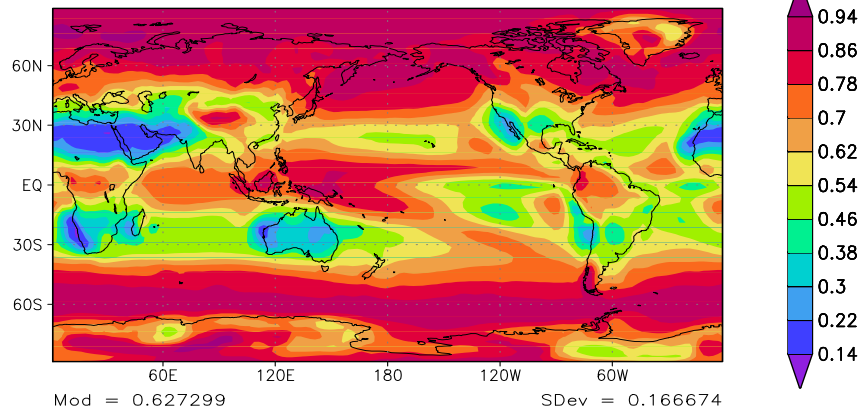


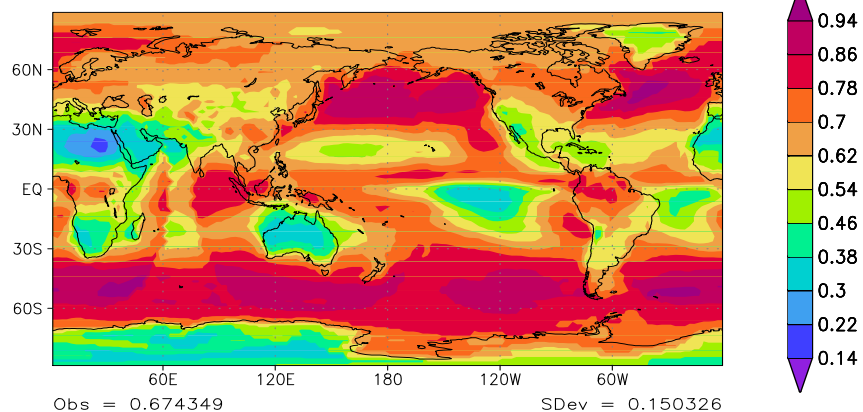
Figure 10. Annual long-term mean absorbed solar radiation (SWAbs) in W m^{-2} for (a) AM2/LM2, (b) ERBE observations, and (c) AM2/LM2 minus ERBE. Statistics at the bottom of (a) and (b) include the global mean and standard deviation. Statistics at the bottom of (c) include the difference in global means, the correlation coefficient, and the root mean square error.

ANN TOTCLDAMT (Amt)

AM2/LM2



ISCCP



AM2/LM2 minus ISCCP

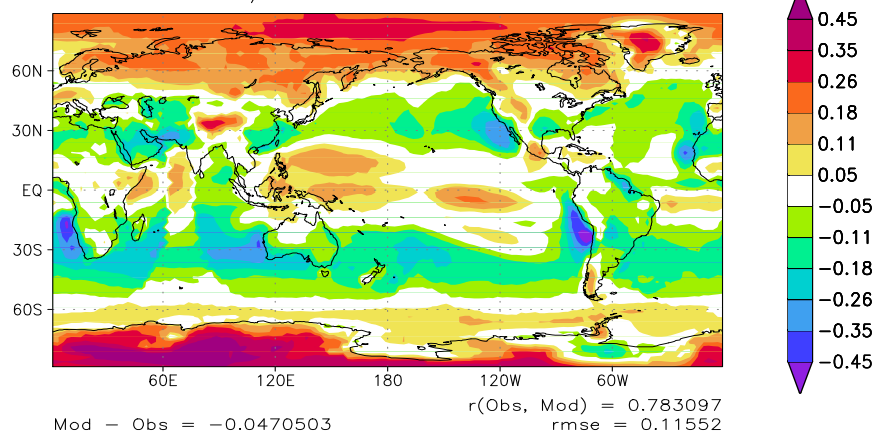


Figure 11. Annual long-term mean total cloud amount (fraction) for (a) AM2/LM2, (b) ISCCP observations, and (c) AM2/LM2 minus ISCCP. Statistics at the bottom of (a) and (b) include the global mean and standard deviation. Statistics at the bottom of (c) include the difference in global means, the correlation coefficient, and the root mean square error. Note that these statistics have been computed only over the domain 60°S-60°N, as high latitude ISCCP data is unreliable.

GFDL GAMDT

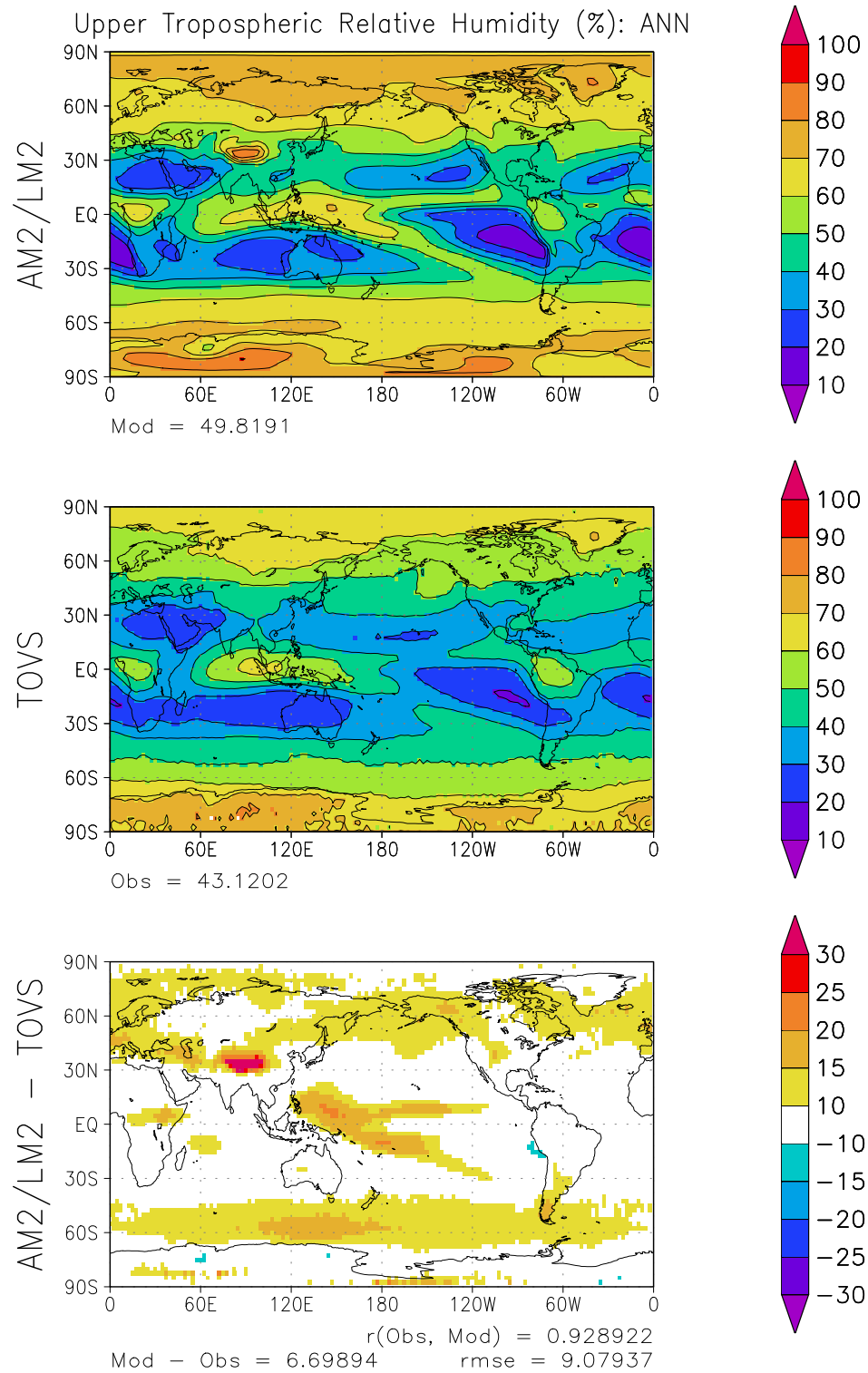
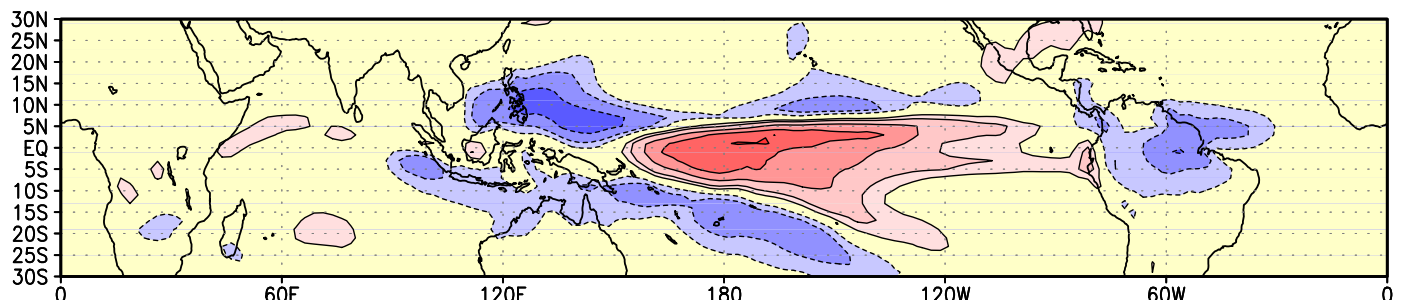


Figure 12. Annual long-term mean upper tropospheric humidity in percent for (a) AM2/LM2, (b) TOVS observations, and (c) TOVS minus AM2/LM2. Statistics at the bottom of (a) and (b) indicate the global mean. Statistics at the bottom of (c) include the difference in global means, the correlation coefficient, and the root mean square error.

AM2/LM2



GPCP Observations

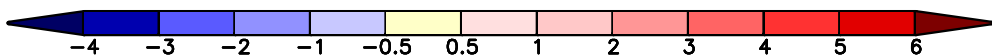
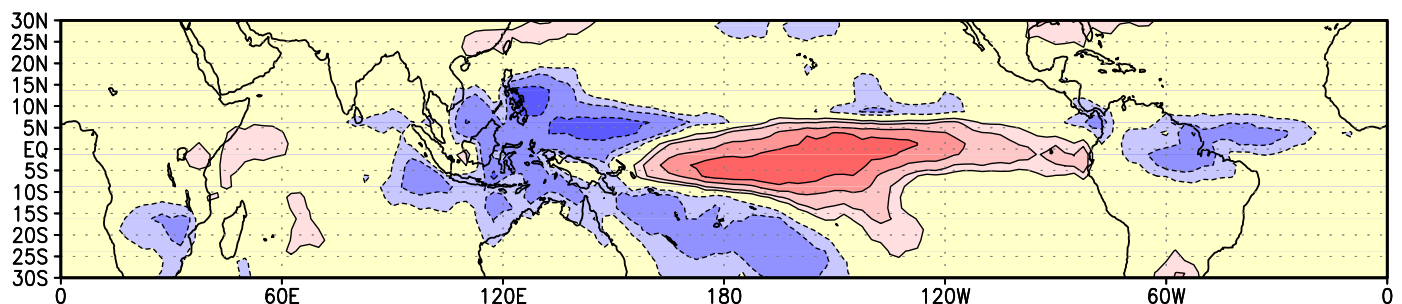
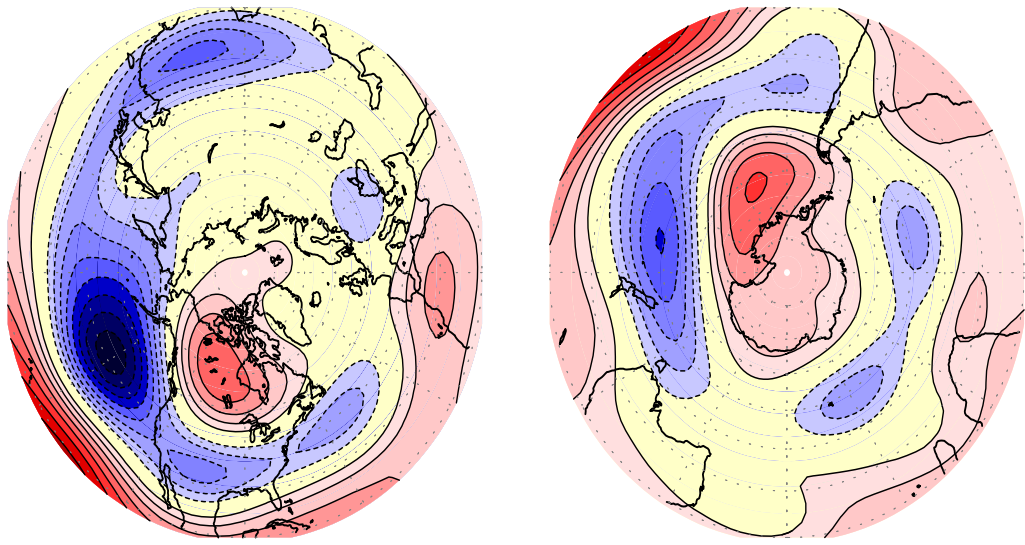


Figure 13. Distributions of the regression coefficients of precipitation rate versus the standardized NINO3 SST index, as computed using the ensemble mean of the 10-member AMIP-style integrations with the AM2/LM2 for 1951-2000 (upper panel) and the GPCP dataset for 1979-2000, both for the December-January-February season. Contour interval: 1 mm d⁻¹. Zero contour is omitted. Contours for -0.5 and +0.5 mm d⁻¹ are inserted.

AM2/LM2



Reanalysis

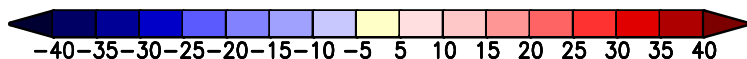
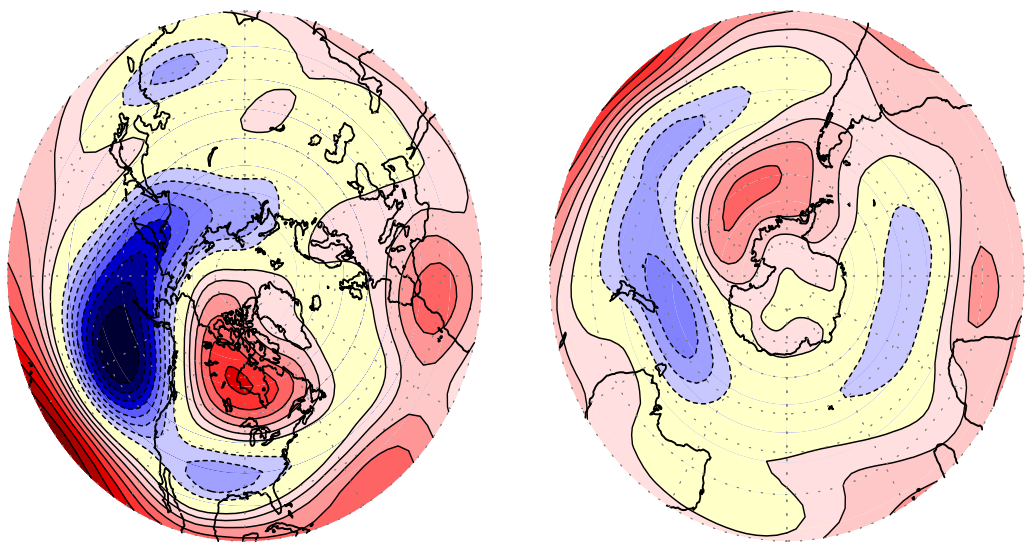


Figure 14. Distributions of the regression coefficients of 200 hPa height versus the standardized NINO3 SST index, as computed using the ensemble mean of the 10-member AMIP-style integrations with the AM2/LM2 (upper panels) and NCEP reanalyses (lower panels) for the December-January-February season of the 1951-2000 period. Results for the northern and southern extratropics are shown in the left and right panels, respectively. Contour interval is 5 m. The zero-contour is not plotted.

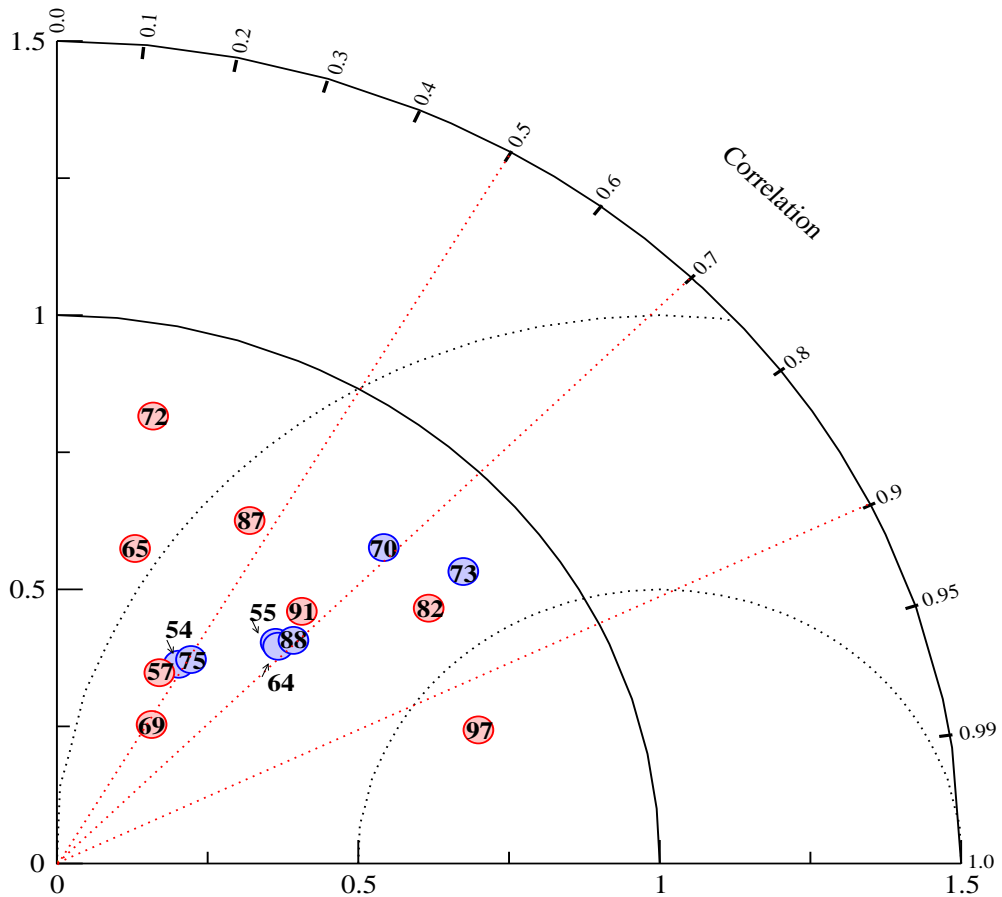


Figure 15. Taylor diagram depicting the relationships between the observed DJF 200 hPa height anomalies in the North Pacific / North American sector (20° - 70° N, 60° - 180° W) during selected ENSO events and the corresponding ensemble-mean patterns as simulated in the 10-member AMIP-style runs with the AM2/LM2. Results for individual warm and cold ENSO events are presented using red and blue dots, respectively. The two-digit label for each dot indicates the year of the event in question. The spatial correlation coefficient is given by the cosine of the angle between the abscissa and the straight line joining the origin and the dot representing the event of interest; correlation values are given along the outer solid arc. The ratio between the simulated and observed spatial variances is given by the distance between the dot and origin; inner and outer solid arcs indicate ratios of 1 and 1.5, respectively. The root mean square (rms) difference between the simulated and observed pattern, as normalized by the spatial variance of the observed field, is given by the distance between the dot and the point with coordinates (1,0) in the diagram; inner and outer dotted arcs indicate normalized rms differences of 0.5 and 1, respectively.

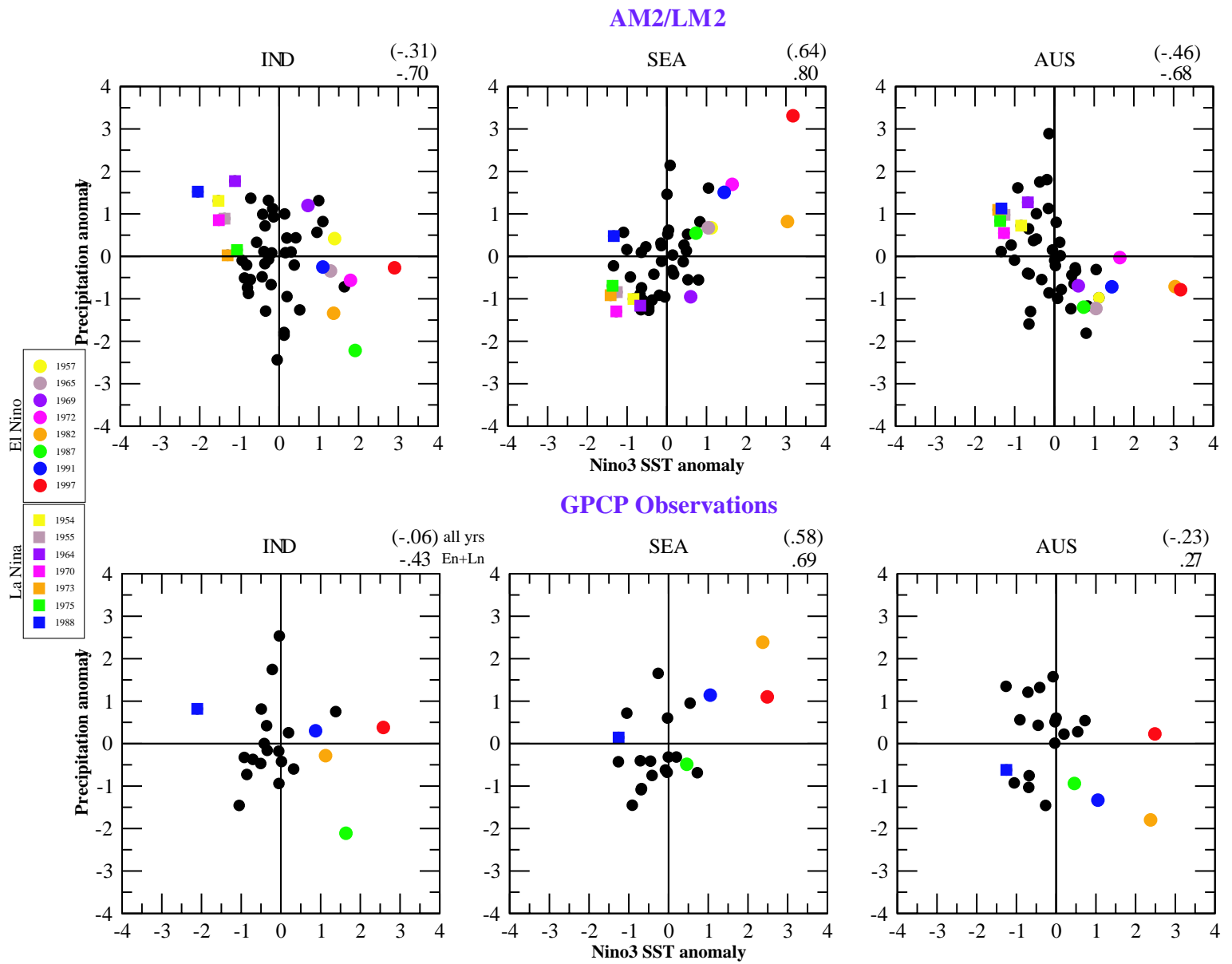


Figure 16. Scatterplots of the precipitation anomalies in three monsoon regions [IND - Indian; AUS - northern Australia; SEA - southeast Asia; boundaries of these regions are depicted in Figure 3 of Lau and Nath (2000)] versus the NINO3 SST anomalies. The abscissa in all panels represents the standardized SST anomaly in the NINO3 region. The ordinate axis represents the standardized precipitation anomaly in IND during the JJA season (left panels), and in SEA (middle panels) and AUS (right panels) during the DJF season. The upper panels are based on AM2/LM2 output for the 1951-2000 period. The lower panels show the observational estimates provided by GPCP for the shorter period of 1979-2000. In each panel, the anomalies of precipitation and NINO3 index for a given year are jointly depicted by a small dot or square. The outstanding warm and cold ENSO events are highlighted using colored dots and squares, respectively. The data for all remaining years are plotted using black dots. The correlation coefficient for the data entries in each panel is shown in the upper right corner of that panel. Correlation values based on all available years are given in parentheses. Correlation values based on the available warm and cold ENSO events only are given without parentheses.

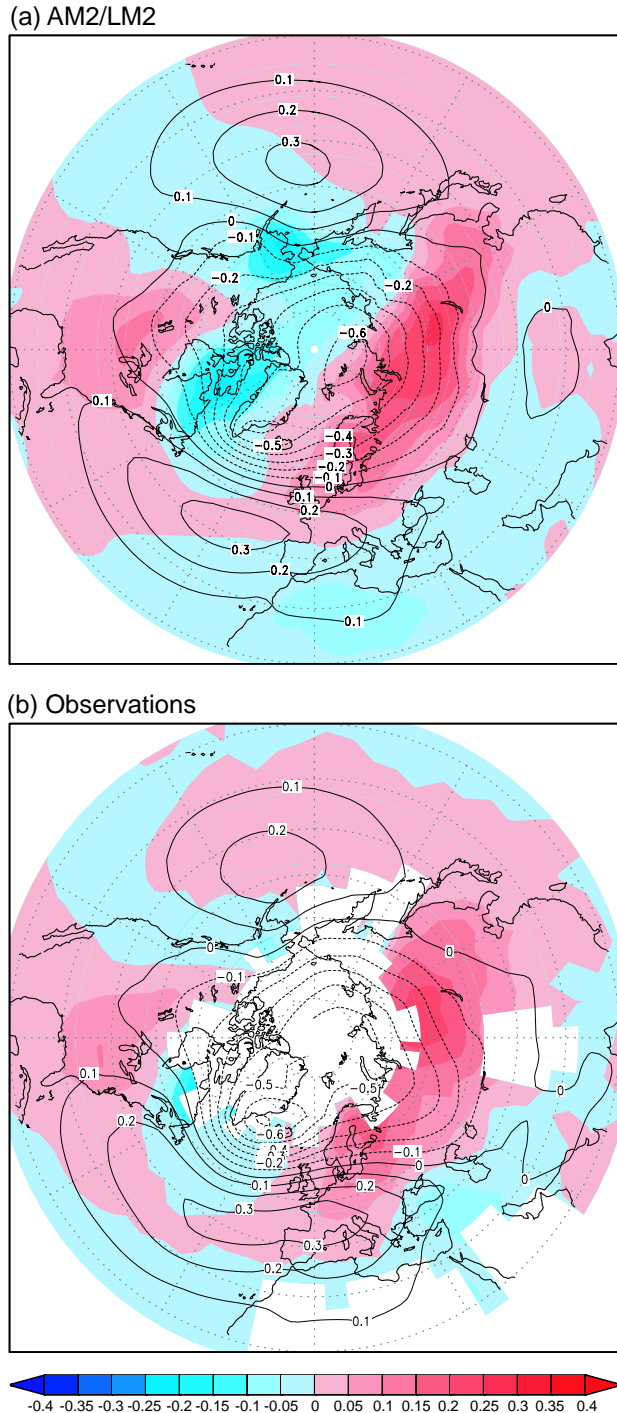


Figure 17. Spatial pattern of anomalies in sea level pressure (SLP, contours) and surface temperature (color shading) associated with a 1 hPa increase in an index of the Northern Annular Mode (NAM), also referred to as the Arctic Oscillation. The anomalies shown are from the months of November through April only. The SLP anomalies are computed by multiplying the linear regression coefficients at each grid point by a 1 hPa increase in a NAM index. The shading indicates the surface air temperature anomalies in °C associated with a 1 hPa increase of a NAM index and is computed in a similar manner. The NAM is defined by computing an empirical orthogonal function (EOF) of SLP for all points north of 20°N. A NAM index is then calculated as the difference between the minimum and maximum of the spatial pattern of the first EOF multiplied by its associated time series, thereby yielding an index with units hPa. (a) Spatial pattern NAM anomalies for AM2/LM2. A 10 member ensemble of experiments was conducted using observed SST variations from 1951 to 2000. For each ensemble member a NAM pattern was computed as described above. The spatial pattern shown is the 10 member ensemble mean of the NAM regression patterns. The temperature shown is the 2 m surface air temperature over both land and ocean. (b) Similar to (a) but for observational data. The EOF of SLP is adapted from Thompson and Wallace, (1998); the surface temperature data is from Jones (1994). Surface air temperature is used over land, while SST is used over oceanic regions including ice-covered areas.

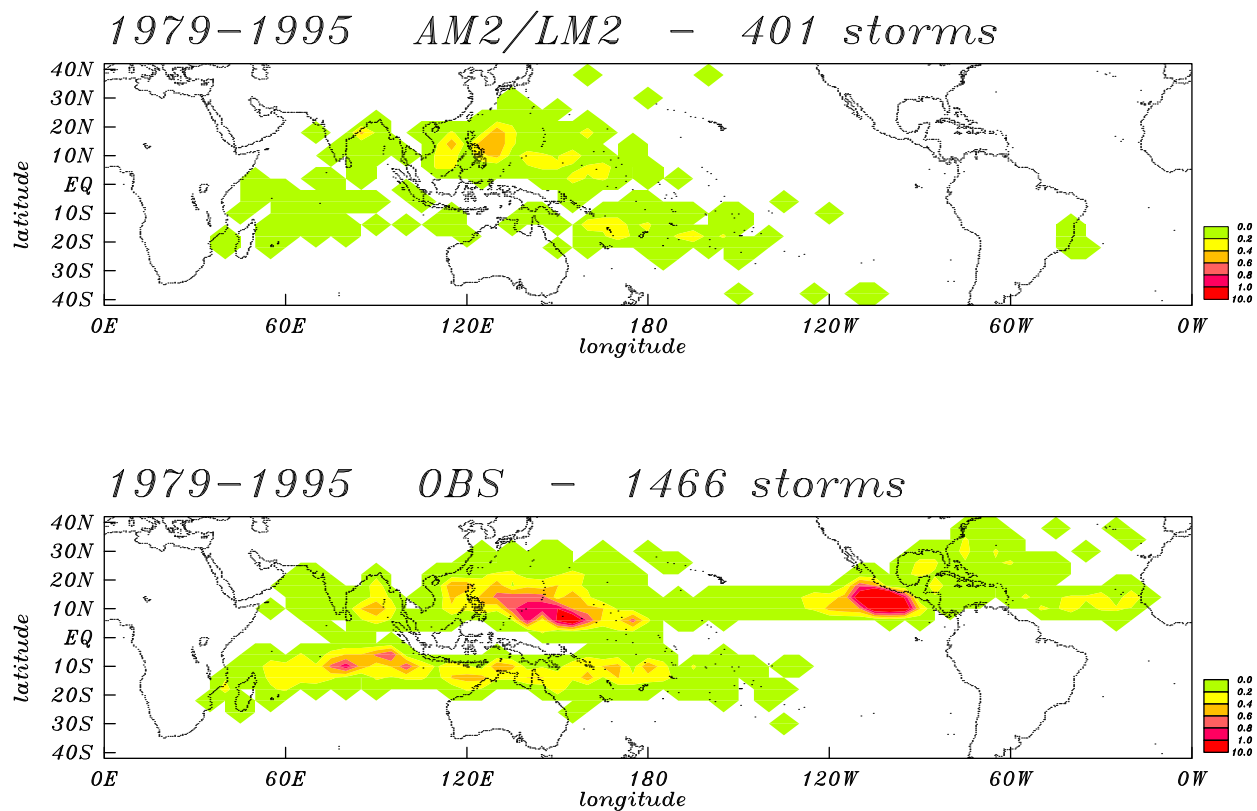


Figure 18. Frequency of tropical cyclone genesis for (a) AM2/LM2 and (b) observations. Units are number of storms per year in a box of size 4° latitude by 5° longitude.

GFDL GAMDT

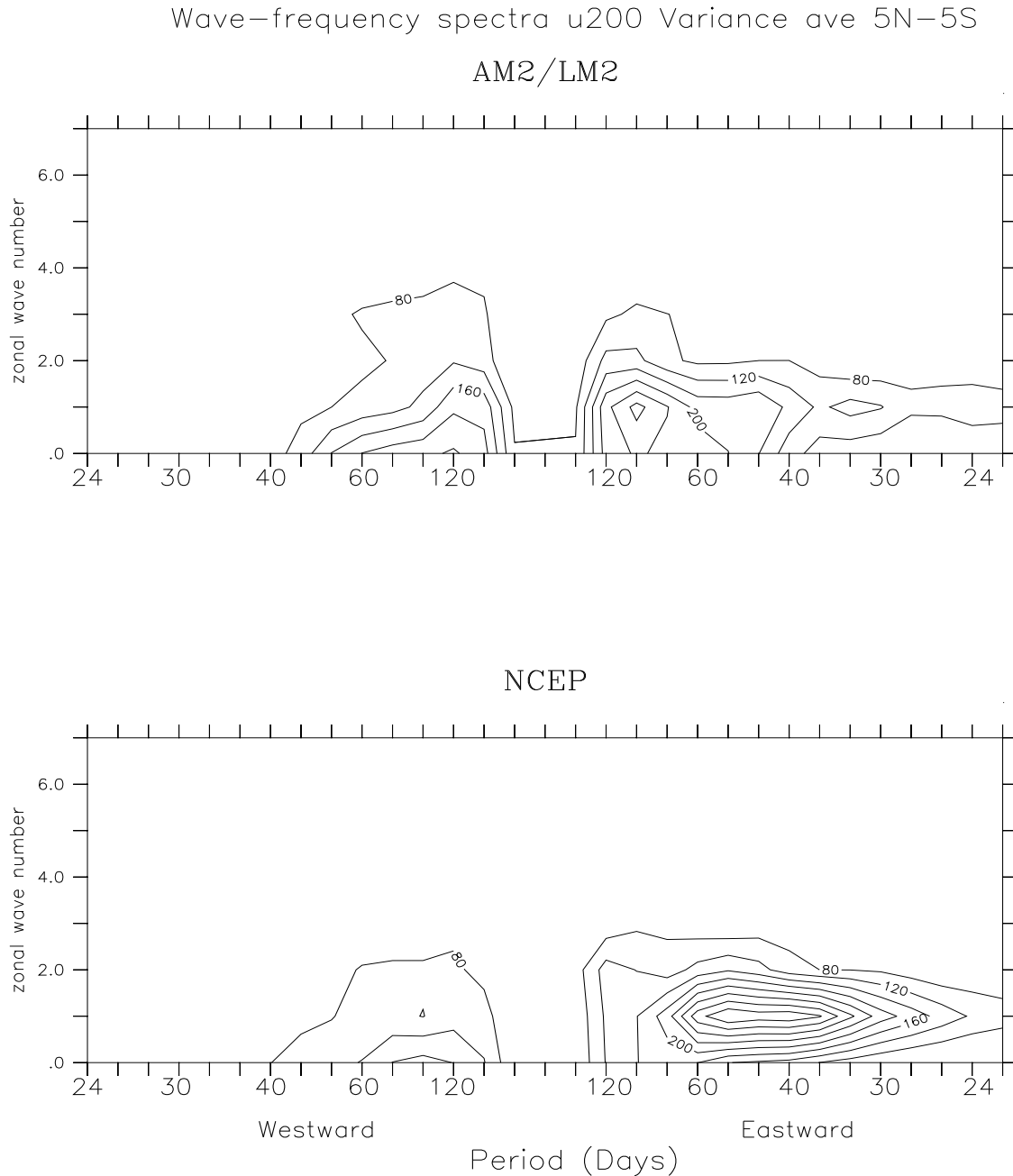


Figure 19. Wave frequency spectra of 5°N to 5°S 200 hPa zonal wind variance for AM2/LM2 (top) and NCEP reanalyses (bottom). Contour interval is 40 m²s⁻².

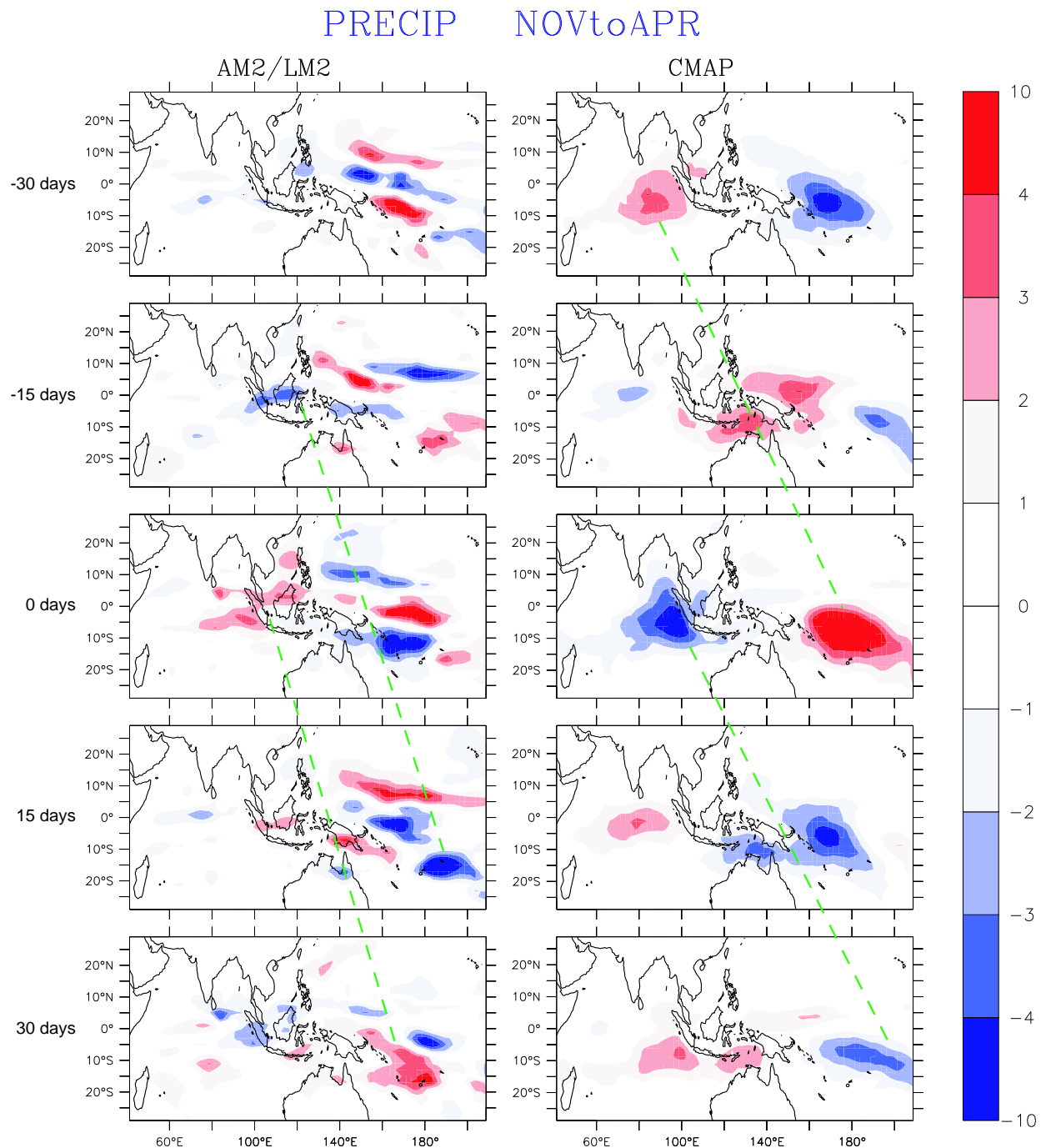


Figure 20. Composite Northern Hemisphere winter (November-April) Madden-Julian Oscillation from 30-90 day filtered precipitation in mm d^{-1} . Maps based on AM2/LM2 are shown in the left column and those based on CMAP observations in right column. Sequential maps are 10 day means centered on lags of -30 days, -15 days, 0 days, +15 days, and +30 days. The superimposed green dashed lines indicate propagation of the disturbance. Note that the values for AM2/LM2 values have been enhanced by a factor of 2.

GFDL GAMDT

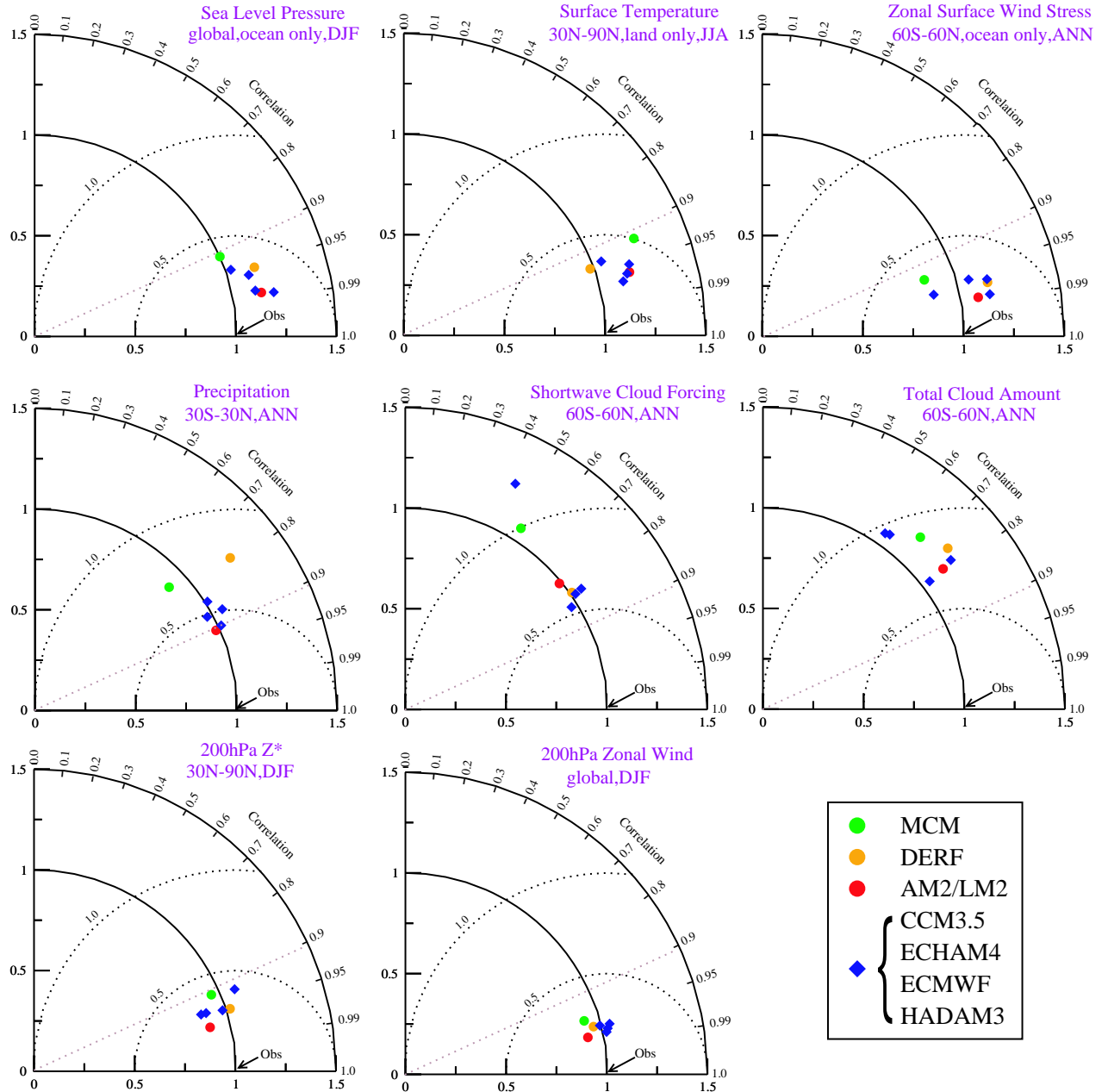


Figure 21. Taylor diagrams for selected variables comparing the skill of AM2/LM2 (red circle) in reproducing the observed climatology to that of older GFDL models (MCM and DERF, green and orange circles respectively) and other models participating in AMIP II (CCM3.5, ECHAM4, ECMWF, and HADAM3). Note that all non-GFDL models are plotted with a blue diamond to prevent unique identification. The selected variables include those associated with surface climate (SLP, land surface air temperature, and oceanic wind stress, top row), water cycle and clouds (precipitation, shortwave cloud forcing, and total cloud amount, middle row), and upper tropospheric circulation (200 hPa eddy geopotential and zonal wind, bottom row). The observational sources for these data include the NCEP reanalyses for SLP and 200 hPa eddy geopotential and zonal wind, ECMWF reanalyses for oceanic wind stress, ERBE for cloud radiative forcing, ISCCP for total cloud amount, CMAP for precipitation and CRU for land surface air temperature. Beneath each variable name is an indication of the geographical domain and season used in the calculation.

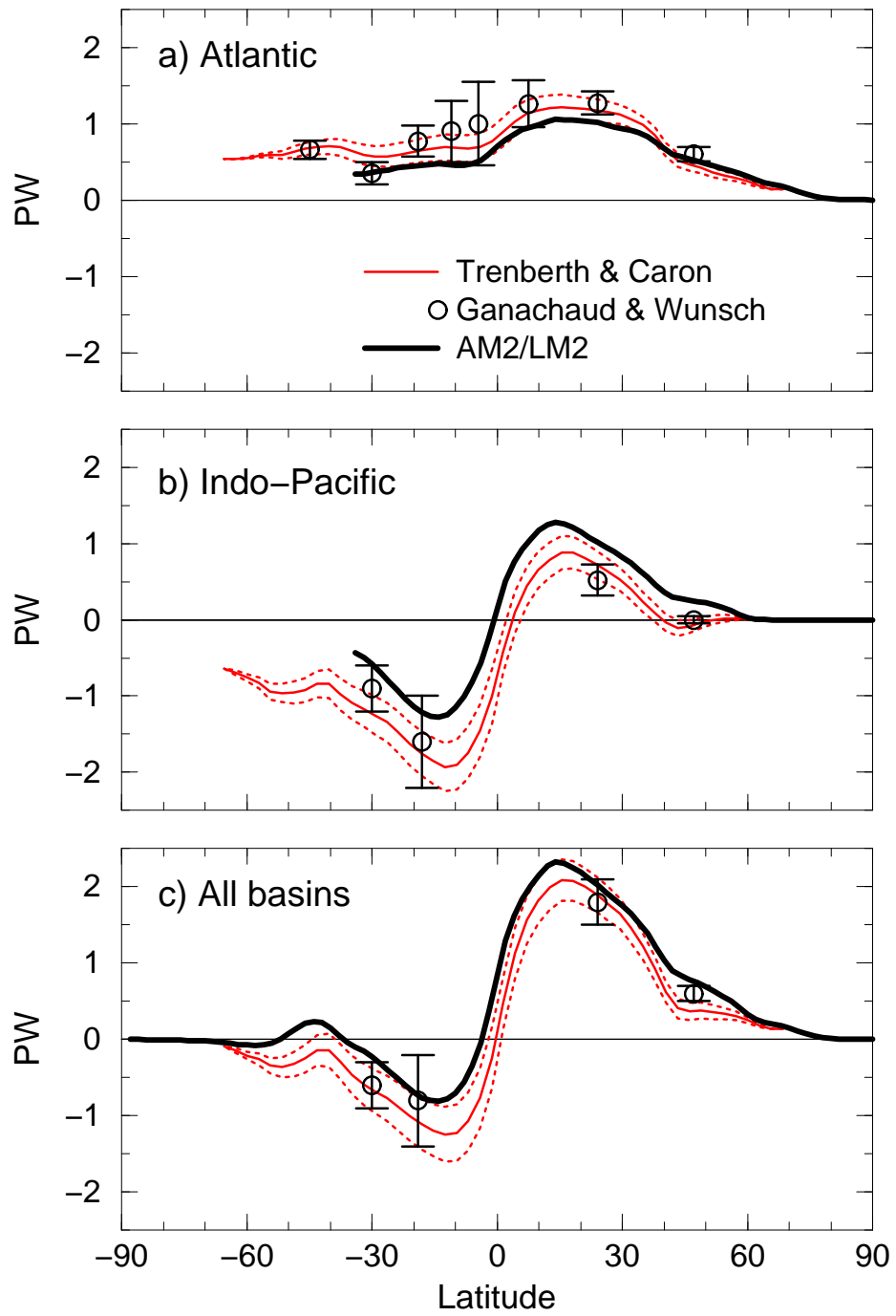


Figure 22. Poleward oceanic heat transport in petawatts (10^{15} W) from observational based estimates and implied by AM2/LM2 (dark black line). The observed estimates are derived from atmospheric data (Trenberth and Caron 2001; red lines with dashed lines indicating plus or minus one standard error; based on NCEP-derived products) or oceanic data (Ganachaud and Wunsch 2003). Results are shown for the a) Atlantic, b) Indo-Pacific, and c) world ocean basins.